PCCP

Optimal control of orientation and entanglement for two dipole-dipole coupled quantum planar rotors

Journal:	*Physical Chemistry Chemical Physics*
Manuscript ID	CP-ART-01-2018-000231.R1
Article Type:	Paper
Date Submitted by the Author:	03-Apr-2018

Complete List of Authors:	YU, Hongling; East China Normal University; Princeton University, Department of Chemistry Ho, Tak-San; Princeton University, Department of Chemistry Rabitz, Herschel; Princeton University, Department of Chemistry

Optimal control of orientation and entanglement for two dipole-dipole coupled quantum planar rotors

Hongling Yu,[1,2] Tak-San Ho,[2,*] and Herschel Rabitz[2,†]

[1]*State Key Laboratory of Precision, East China Normal University, Shanghai 200062, China*

[2]*Department of Chemistry, Princeton University, Princeton, NJ, USA*

(Dated: revised April 3, 2018)

Abstract

Optimal control simulations are performed for orientation and entanglement of two dipole-dipole coupled identical quantum rotors. The rotors at various fixed separations lie on a model non-interacting plane with an applied control field. It is shown that optimal control of orientation or entanglement represents two contrasting control scenarios. In particular, the maximally oriented state (MOS) of the two rotors has a zero entanglement entropy and is readily attainable at all rotor separations. Whereas, the contrasting maximally entangled state (MES) has a zero orientation expectation value and is most conveniently attainable at small separations where the dipole-dipole coupling is strong. It is demonstrated that the peak orientation expectation value attained by the MOS at large separations exhibits a long time revival pattern due to the small energy splittings arising form the extremely weak dipole-dipole coupling between the degenerate product states of the two free rotors. Moreover, it is found that the peak entanglement entropy value attained by the MES remains largely unchanged as the two rotors are transported to large separations after turning off the control field. Finally, optimal control simulations of transition dynamics between the MOS and the MES reveal the intricate interplay between orientation and entanglement.

* tsho@princeton.edu

† hrabitz@princeton.edu

I. INTRODUCTION

With advances in quantum optimal control theory (OCT) [1–3] and efficient monotonically convergent search algorithms [4–9], optimal control of quantum dynamics has become an active research field both theoretically and computationally, with a wide range of applications including chemical reactions [10, 11], molecular focusing [12], high-harmonic generation [13] and quantum information processing[14]. In particular, applications of OCT and monotonically convergent algorithms to molecular orientation [15–18] have attracted much attention in recent years. For example, Hoki and Fujimura [15] showed that the orientation of CO molecules can be optimally controlled by taking into account both the dipole moment and polarizability. Salomon et al. [16] found that optimal molecular orientation of HCN can be achieved through rotational ladder climbing using an optimal field in the microwave regime. Liao et al. [17] showed that a nearly maximal degree of orientation of OCS can be achieved by using strong near-single-cycle pulses. Ohtsuki et al. [18] demonstrated the control of molecular orientation with an optimal combination of THz and laser pulses. In this regard, many successful experiments on the field-free orientation of polar molecules have been carried out with various laser setups in the past decade, for example, by combining an intense nonresonant rapidly turned-off shaped laser field with a static electric field [19], using single-cycle THz laser pulses [20], employing strong picosecond THz laser pulses [21], and combining a weak static electric field with a moderately intense nano-to-sub-nanosecond-long nonresonant laser pulse [22]. In addition, enhancement of angular alignment of single quantum rotors using specially designed pulse sequences have been experimentally realized in optical lattices [23]. However, all of these studies only considered isolated polar molecules.

The dipole-dipole coupled two-rotor system has attracted recent interest. For example, Shima and Nakayama [24] explored the anomalous dielectric response of two quantum rotors and showed that the dipole-dipole interaction between the rotors can enhance orientation using ultrashort laser pulses. Other studies focused on generating entanglement among coupled rotors, since it is an important feature for implementation of quantum information processing [25]. For example, Hettich et al. [26] have shown that the strong dipole-dipole interaction between two individual molecules can create entangled states by applying a differential Stark shift via an inhomogeneous electric field. Moreover, the entanglement of dipole coupled diatoms under strong laser fields was investigated by Liao et al. [27], showing that entanglement can be enhanced by applying multiple laser pulses. In addition, Charron et al. [28] proposed effective schemes for quantum phase gate pro-

duction and entanglement generation between rotational quantum states of two polar molecules using a sequence of laser pulses that simultaneously excite both molecules. Recently, optimal control theory has also been applied to coupled polar molecules for implementing basic quantum logic gates [29, 30]. In the laboratory, dipole-dipole coupled rotors may be adsorbed on a weakly interacting solid surface [26, 31], trapped in an optical lattice [28, 32, 33], or prepared in deeply bound ground states using molecular cooling techniques [34, 35].

In this work, we study optimal control of either orientation or entanglement of two planar quantum rotors coupled by the dipole-dipole interaction using gradient-based D-MORPH method [36, 37] to find the control field. The D-MORPH method has proved to be efficient and robust for finding optimal control fields in diverse applications, including open quantum systems [37], the nonlinear Schrödinger equation [38], and classical dynamics [39], as well as with temporal and frequency constraints on the control fields [40]. The orientation and entanglement optimal control problems represent two contrasting control scenarios. At one extreme, the maximally oriented state (MOS) completely disentangles the two rotors, while at the other extreme, the maximally entangled state (MES) [41] possesses a zero expectation value for orientation. The goal of the present study is to find optimally shaped control fields to reach either the MOS or the MES at a specified final time τ_f. In this regard, there is available state-of-the-art technology for generation of microwave arbitrary waveform generation [43]. We note that both the orientation and entanglement optimization objectives, assuming a pure initial state, can be cast as state-to-state optimal control problems. This circumstance is important since the latter pure-state objective functionals correspond to the state-to-state transition probability control landscapes, which are expected to almost always have no local-traps or saddles [44, 45]. In addition to achieving entanglement via optimal control, we will also examine if entanglement can be maintained by allowing the two rotors to be transported to large separations with various speeds after turning off the control field. Finally, we will also investigate the interplay of optimal control transition dynamics between the MOS and the MES.

The remainder of this paper is organized as follows. Section II provides a general description of optimal control of two interacting identical polar rotors, including the model Hamiltonian, the time-dependent equations for evolution of the wave function, definitions of the MOS and MES, and the gradient-based D-MORPH method for the optimization of the control. Section III presents numerical results for optimal control of orientation and entanglement, including field-free evolution of orientation and transport of entanglement, and optimal transition dynamics between the

MOS and MES. Concluding remarks are presented in Sec. IV. In addition, Appendices A, B, C and D provide detailed mathematical analyses complementing the material in the main text.

II. THEORETICAL FOUNDATIONS

A. Model Hamiltonian

Consider two identical, linear polar quantum rotors that lie in a plane at a fixed separation R and controlled by a linearly polarized time-dependent field $\varepsilon(t)$ along the $\hat{\mathbf{x}}$-axis, as shown in Fig. 1. Within the electric dipole approximation, the total Hamiltonian of such a two-rotor quantum system can be written as

$$H(t) \equiv H_0 - \mu[\cos\varphi_1 + \cos\varphi_2]\varepsilon(t), \tag{1}$$

where

$$H_0 = B\left(L_1^2 + L_2^2\right) + W_{12}. \tag{2}$$

is the field-free coupled rotor Hamiltonian and $\varphi_1 \in [-\pi, \pi]$ and $\varphi_2 \in [-\pi, \pi]$, respectively, are angles between the dipole moment $\boldsymbol{\mu}_1$ and $\boldsymbol{\mu}_2$ with ($|\boldsymbol{\mu}_1| = |\boldsymbol{\mu}_2| = \mu$) and the electric field $\varepsilon(t)$. Here, $L_j^2 = -\hbar^2\partial^2/\partial\varphi_j^2$ ($j = 1, 2$) are the angular momentum operators of the individual free planar rotors, $B = 1/2I$ is the rotational constant, with I the moment of inertia of an individual rotor, and

$$\begin{aligned} W_{12} &\equiv W_{12}(R, \theta, \varphi_1, \varphi_2) \\ &= \frac{\boldsymbol{\mu}_1 \cdot \boldsymbol{\mu}_2 - 3\left(\boldsymbol{\mu}_1 \cdot \hat{\mathbf{R}}\right)\left(\boldsymbol{\mu}_2 \cdot \hat{\mathbf{R}}\right)}{4\pi\epsilon_0 R^3} \\ &= \frac{\mu^2}{4\pi\epsilon_0 R^3} \times \left[\cos(\varphi_1 - \varphi_2) - 3\cos(\varphi_1 - \theta)\cos(\varphi_2 - \theta)\right] \end{aligned} \tag{3}$$

is the dipole-dipole interaction between the two rotors, with ϵ_0 being the vacuum permittivity, R is the separation between two rotors, and $\theta \in [0, \pi/2]$ is the configuration angle lying between the inter-rotor vector $\mathbf{R} \equiv R\hat{\mathbf{R}}$ and the electric field $\varepsilon(t)$. In the case of orientation as the goal, the angle $\alpha \in [-\pi/2, \pi/2]$ is the designated target orientation for both rotors.

To facilitate the analysis, we choose the dimensionless time $\tau = B\hbar t$ and the new energy unit $B\hbar^2$ in the remainder of the paper. The resultant dimensionless total Hamiltonian in Eq.(1) can then be cast as (hereafter $\hbar = 1$)

$$\widetilde{H}(\tau) = \left\{\left(L_1^2 + L_2^2\right) + \widetilde{W}_{12}\right\} + \widetilde{V}(\tau), \tag{4}$$

where the dimensionless time is $\tau = Bt$, the dimensionless dipole-dipole interaction is

$$\begin{aligned}\widetilde{W}_{12} &\equiv \widetilde{W}_{12}(R,\theta,\varphi_1,\varphi_2) \\ &\equiv \frac{W_{12}(R,\theta,\varphi_1,\varphi_2)}{B} \\ &= \Gamma\left[\cos(\varphi_1-\varphi_2) - 3\cos(\varphi_1-\theta)\cos(\varphi_2-\theta)\right], \end{aligned} \tag{5}$$

and the dimensionless dipole-control field interaction is

$$\widetilde{V}(\tau) = -\frac{\mu}{B} \times \varepsilon(\tau) \times [\cos\varphi_1 + \cos\varphi_2], \tag{6}$$

with the dimensionless dipole-dipole coupling parameter

$$\Gamma = \frac{E_D}{B} \tag{7}$$

denoting the ratio of the dipole-dipole coupling strength $E_D = \mu^2 \Big/ \left(4\pi\epsilon_0 R^3\right)$ and the rotational constant B (which is equal to the energy difference between the lowest and the first excited levels of each individual free planar rotor).

The wave function $|\psi(\tau)\rangle$ of the coupled rotors in the presence of a laser field is governed by the time-dependent Schrödinger equation

$$i\frac{\partial|\psi(\tau)\rangle}{\partial\tau} = \widetilde{H}(\tau)|\psi(\tau)\rangle, . \tag{8}$$

To solve Eq. (8), the wave function $|\psi(\tau)\rangle$ may be expanded as

$$|\psi(\tau)\rangle = \sum_{k=1}^{(2M+1)\times(2M+1)} |E_k\rangle\langle E_k|\psi(\tau)\rangle, \tag{9}$$

in terms of the eigenstates $|E_k\rangle$'s of the field-free coupled-rotor Hamiltonian $\widetilde{H}_0$, where

$$\widetilde{H}_0 = \left(L_1^2 + L_2^2\right) + \widetilde{W}_{12} \tag{10}$$

and

$$\widetilde{H}_0|E_k\rangle = E_k|E_k\rangle, \quad k = 1,\cdots(2M+1)\times(2M+1). \tag{11}$$

Alternatively, the wave function may be expanded as

$$|\psi(\tau)\rangle = \sum_{m_1=-M}^{M}\sum_{m_2=-M}^{M} |m_1 m_2\rangle\langle m_1 m_2|\psi(\tau)\rangle \tag{12}$$

in terms of the direct products $|m_1 m_2\rangle \equiv |m_1\rangle \otimes |m_2\rangle$ of the eigenstates $|m_1\rangle$ of L_1^2 and $|m_2\rangle$ of L_2^2, where M is a sufficiently integer number for the particular application, and $\otimes$ denotes the direct product. The eigenstates $\left|m_j\right\rangle$, $j = 1, 2$, satisfy the equation

$$L_j^2 \left|m_j\right\rangle = m_j^2 \left|m_j\right\rangle, m_j = -M, \cdots -1, 0, 1, \cdots + M, \tag{13}$$

and the orthonormal relations

$$\langle m_j | m_j' \rangle = \delta_{m_j, m_j'}. \tag{14}$$

Moreover, we may express each eigenstate $|m_j\rangle$ in terms of the rotor angles φ_j as

$$\langle \varphi_j | m_j \rangle \equiv \frac{1}{\sqrt{2\pi}} \exp\left(i m_j \varphi_j\right), \tag{15}$$

which immediately leads to the relation

$$\langle m_j | \cos\varphi_j | m_j' \rangle = \frac{1}{2}\left\{\delta_{m_j, m_j'-1} + \delta_{m_j, m_j'+1}\right\}, \tag{16}$$

showing that the dipole-field coupling, Eq. (6), only links the nearest adjacent rotational levels. Finally, it is noted that a two-dimensional (2D) planar rotor is characterized by a revival time equal to the rotational period $T_{\rm rot} = 2\pi/B$ (or $\tau_{\rm rot} = BT_{\rm rot} = 2\pi$ in the dimensionless time), which is twice of the rotational period π/B of its three-dimensional (3D) counterpart.

B. Maximally Oriented State

The joint orientation operator of two coupled rotors associated with an arbitrary target angle α, is given as

$$\hat{O}(\alpha) \equiv \cos(\varphi_1 + \alpha) + \cos(\varphi_2 + \alpha). \tag{17}$$

The MOS $|\psi_{\rm MOS}\rangle$ of the coupled rotors in their finite basis set may be identified as the eigenstate $|\lambda_{\max}(\alpha)\rangle$ associated with the largest eigenvalue $\lambda_{\max} = 2\cos\left(\frac{\pi}{2M+2}\right)$ (see Appendix A) of the joint orientation operator $\hat{O}(\alpha)$, i.e.,

$$|\psi_{\rm MOS}\rangle \equiv |\lambda_{\max}(\alpha)\rangle \tag{18}$$

and

$$\{\cos(\varphi_1 + \alpha) + \cos(\varphi_2 + \alpha)\}\,|\lambda_{\max}(\alpha)\rangle = \lambda_{\max}(\alpha)|\lambda_{\max}(\alpha)\rangle. \tag{19}$$

In the limit $M = \infty$ we find $\lambda_{\max} = \lim_{M\to\infty} 2\cos\left(\frac{\pi}{2M+2}\right) = 2$. In the optimal control calculations, we chose $M = 8$, which yields a maximum eigenvalue $\lambda_{\max} = 1.97$.

It is noted that since the operator $\hat{O}(\alpha)$ is a linear summation of single-rotor orientation operators $\cos(\varphi_1+\alpha)$ and $\cos(\varphi_2+\alpha)$, the MOS $|\lambda_{\max}(\alpha)\rangle$, Eq. (18), of the coupled rotors can be written as the direct product (see Eqs. (A6) - (A15)):

$$|\lambda_{\max}(\alpha)\rangle = \left|\lambda^{[1]}_{\max}(\alpha)\right\rangle \otimes \left|\lambda^{[2]}_{\max}(\alpha)\right\rangle, \tag{20}$$

where the MOSs $\left|\lambda^{[1]}_{\max}(\alpha)\right\rangle$ and $\left|\lambda^{[2]}_{\max}(\alpha)\right\rangle$ are the eigenstates, respectively, associated with the largest eigenvalues $\lambda^{[1]}_{\max} = \lambda^{[2]}_{\max} = \cos\left(\frac{\pi}{2M+2}\right)$ of the uncoupled rotors 1 and 2, satisfying the eigenvalue relations (see Eqs. (A1) - (A4))

$$\cos\left(\varphi_j+\alpha\right)\left|\lambda^{[j]}_{\max}(\alpha)\right\rangle = \lambda^{[j]}_{\max}\left|\lambda^{[j]}_{\max}(\alpha)\right\rangle, \ j=1,2, \tag{21}$$

with $\cos(\varphi_i+\alpha)$ being approximated as a $(2M+1)\times(2M+1)$ matrix in the Hilbert space spanned by the free-rotor eigenstates $\{|m_i\rangle\}$. We remark that the MOS $|\lambda_{\max}(\alpha)\rangle$ is independent of the rotor-rotor separation R (i.e., independent of the dipole-dipole coupling $\widetilde{W}_{12}$, Eq. (5)), as well as the dipole moment μ, the rotational constant B, and the control field $\varepsilon(\tau)$, cf. Eq. (6). Finally, the process of controlling the joint orientation with an optimal field $\varepsilon(\tau)$ can be equivalently regarded as optimizing the transition probability from a given initial state $|\psi(0)\rangle$ to the MOS $|\psi_{\rm MOS}\rangle$. In this context, the target observable for the orientation optimization can be written as a pure state projection operator

$$\hat{O}_{\rm MOS} \equiv |\psi_{\rm MOS}\rangle\langle\psi_{\rm MOS}|, \tag{22}$$

which is expected to be associated with a trap-free control landscape [44, 45].

C. Maximally Entangled State

The degree of entanglement for the coupled rotors can be determined by the von Neumann entropy $S_{\rm vN}(|\psi(\tau)\rangle)$ defined as [41]

$$S_{\rm vN}(|\psi(\tau)\rangle) \equiv -{\rm Tr}\left\{\rho_1(\tau)\ln\rho_1(\tau)\right\}, \tag{23}$$

where the reduced density matrix $\rho_1(\tau)$ is defined as $\rho_1(\tau) \equiv {\rm Tr}_2\left\{|\psi(\tau)\rangle\langle\psi(\tau)|\right\}$, which is the partial trace over the rotor 2. Here the index 1 can be equivalently exchanged with 2. The MES of the system of two coupled identical rotors can be written as [41]

$$\begin{aligned}|\psi_{\rm MES}\rangle &= \sqrt{\frac{1}{2M+1}}\sum_{m=-M}^{M}|m\rangle\otimes|m\rangle \\ &= \sqrt{\frac{1}{2M+1}}\left\{|0\rangle\otimes|0\rangle + \sum_{m=1}^{M}\left[|m\rangle\otimes|m\rangle + |-m\rangle\otimes|-m\rangle\right]\right\},\end{aligned} \tag{24}$$

with the maximal entanglement (von Neumann) entropy

$$S_{\mathrm{vN}}(|\psi_{\mathrm{MES}}\rangle) = \ln(2M+1). \tag{25}$$

The optimal control goal in this case is to find a properly shaped laser field $\varepsilon(\tau)$ for steering the coupled rotors from an arbitrary initial state $|\psi(0)\rangle$ to reach the MES $|\psi_{\mathrm{MES}}\rangle$. The target observable for the entanglement optimization can be conveniently written as the projection operator

$$\hat{O}_{\mathrm{MES}} \equiv |\psi_{\mathrm{MES}}\rangle\langle\psi_{\mathrm{MES}}|. \tag{26}$$

It is straightforward to prove the following properties: (i) the MES possesses a zero expectation value of orientation, i.e.,

$$\begin{aligned}
&\langle\psi_{\mathrm{MES}}|\hat{O}(\alpha)|\psi_{\mathrm{MES}}\rangle \\
&= \frac{1}{2M+1}\sum_{m}\sum_{m'}\left(\langle m|\cos(\varphi_1+\alpha)\left|m'\right\rangle + \langle m|\cos(\varphi_2+\alpha)\left|m'\right\rangle\right)\delta_{m,m'} \\
&= 0,
\end{aligned} \tag{27}$$

(ii) in the absence of the control field the MES yields a zero expectation value of the orientation operator (see Appendix B), i.e.,

$$\langle\psi_{\mathrm{MES}}(\tau)|\hat{O}(\alpha)|\psi_{\mathrm{MES}}(\tau)\rangle = 0 \tag{28}$$

for all $\tau > 0$, where $|\psi_{\mathrm{MES}}(0)\rangle$=$|\psi_{\mathrm{MES}}\rangle$, and (iii) from Appendix A, all eigenstates $\left|\lambda_{k_1}^{[1]}(\alpha)\right\rangle \otimes \left|\lambda_{k_2}^{[2]}(\alpha)\right\rangle$, including the MOS $|\lambda_{\max}(\alpha)\rangle = \left|\lambda_{\max}^{[1]}(\alpha)\right\rangle \otimes \left|\lambda_{\max}^{[2]}(\alpha)\right\rangle$ of the orientation operator $\hat{O}(\alpha)$ are separable, thus have zero entanglement entropy, i.e.,

$$S_{\mathrm{vN}}\left(\left|\lambda_{k_1}^{[1]}(\alpha)\right\rangle \otimes \left|\lambda_{k_2}^{[2]}(\alpha)\right\rangle\right) = 0 \;\forall k_1, k_2 = 1, \cdots, 2M+1. \tag{29}$$

D. Optimization scheme: the gradient-based D-MORPH method

A general objective of quantum optimal control simulations in this paper is to find a control field $\varepsilon(\tau)$ that produces the maximum value of an objective functional $J\left(\tau_f\right)$ associated with either the orientation or entanglement of the two coupled rotors at the final time τ_f. Specifically, starting from the initial state $|\psi(0)\rangle$, the corresponding optimal control problems can be expressed as

$$\max_{\varepsilon(\tau)} J\left(\tau_f\right) = \left\langle\psi\left(\tau_f\right)\right|\hat{O}\left|\psi\left(\tau_f\right)\right\rangle, \tag{30}$$

where $|\psi(\tau_f)\rangle$ is the final state of the coupled rotors generated by the optimal control field at the terminal time τ_f and $\hat{O}$ is either the joint orientation operator $\hat{O} = \cos(\varphi_1 + \alpha) + \cos(\varphi_2 + \alpha)$ for orientation control, Eq. (17), or $\hat{O} = |\psi_{\mathrm{MES}}\rangle\langle\psi_{\mathrm{MES}}|$ for entanglement control, Eq.(26).

In order to find an optimal field, we utilize the gradient-based D-MORPH method [36, 37]. Specifically, the control field $\varepsilon(\tau)$ is parametrized by a morphing variable $s \geq 0$ resulting in $\varepsilon(s,\tau)$. Then the D-MORPH differential equation

$$\frac{\partial\varepsilon(s,\tau)}{\partial s} = \frac{\delta J}{\delta\varepsilon(s,\tau)} \tag{31}$$

is solved, given an initial control field $\varepsilon(0,\tau)$, where the gradient $\delta J/\delta\varepsilon(s,\tau)$ can be written as

$$\frac{\delta J}{\delta\varepsilon(\tau)} = -\frac{2\mu}{B} \times \mathrm{Im}\langle\chi(\tau)|\hat{O}|\psi(\tau)\rangle. \tag{32}$$

with the co-state function $|\chi(\tau)\rangle$ governed by the time-dependent equation

$$i\frac{\partial|\chi(\tau)\rangle}{\partial\tau} = \hat{H}(\tau)|\chi(\tau)\rangle,\ |\chi(\tau_f)\rangle = \hat{O}|\psi(\tau_f)\rangle. \tag{33}$$

The D-MORPH equation, Eq. (31), can be integrated from $s = 0$, in conjunction with Eqs. (8) and (33), until the objective functional J reaches a maximum, i.e., when the gradient $\delta J/\delta\varepsilon(s,\tau)$ becomes zero (to some acceptable tolerance). The D-MORPH method is always monotonically convergent, i.e.,

$$\frac{dJ}{ds} = \int_0^{\tau_f} \frac{\delta J}{\delta\varepsilon(s,\tau)}\frac{\delta\varepsilon(s,\tau)}{\delta s}d\tau = \int_0^{\tau_f}\left[\frac{\delta J}{\delta\varepsilon(s,\tau)}\right]^2 d\tau \geq 0. \tag{34}$$

The optimization solution of the D-MORPH equation, Eq. (31), is determined by the gradient, Eq. (32), of the underlying control objective functional $J(\tau_f)$, Eq. (30). In all our simulations, Eq. (31) is integrated using an efficient fifth-order Runge-Kutta method [42].

The D-MORPH method, like all other monotonically convergent local optimization methods [4–8], often exhibits asymptotically slow convergence behavior when approaching the maximum, as shown in Fig. 2. All monotonically convergent optimizations generally follow a Sigmoidal curve. For example, a poorly chosen initial control field (e.g., a field with inadequate spectral bandwidth or having too weak intensity) will generally render a full Sigmoidal curve (i.e., requiring more iterations), while a well chosen initial field will likely result in just having the upper portion of the Sigmoidal curve (i.e., exhibiting the need for fewer iterations, which is the case in all our simulations).

III. NUMERICAL SIMULATIONS

In this work, for illustration, we consider two identical dipole-dipole coupled linear OCS rigid rotors (each endowed with a rotational constant $B = 0.203$ cm^{-1} [46] and a dipole moment $\mu = 0.709$ Debye [47]). The corresponding dimensionless time is $\tau = Bt$, with $B^{-1} \approx 26.1$ ps, thus producing a rotational period of $T_{\rm rot} = 2\pi/B \approx 164$ ps (corresponding to the fundamental rotation frequency ≈ 6.09 GHz), for the OCS molecule. For optimal control simulations, the maximal rotational quantum number M is set to 8 and the initial laser control field $\varepsilon(0,\tau)$ is given as

$$\varepsilon(0,\tau) = f(\tau) \times \widetilde{\varepsilon}_0(\tau), \tag{35}$$

which is the product of a Gaussian envelope function

$$f(\tau) = \exp\left[-\ln 4 \times (\tau - \tau_f/2)^2 \Big/ \left(\Delta\tau_p\right)^2 \right] \tag{36}$$

and a time-dependent carrier function (comprising three carrier frequencies)

$$\widetilde{\varepsilon}_0(\tau) = a_0 \left[0.5\cos\omega_1\tau + 0.3\cos\omega_2\tau + 0.2\cos\omega_3\tau\right], \tag{37}$$

where a_0, τ_f, ω_1, ω_2 and ω_3, respectively, denote the amplitude, pulse length, and carrier frequencies of the initial control pulses $\varepsilon(0,\tau)$. In addition, the carrier frequencies ω_1, ω_2 and ω_3 are arbitrarily weighted, here with the numbers 0.5, 0.3, and 0.2. The amplitude of all initial fields is fixed at the value $a_0 = 0.85625 \times 10^5$ V/cm, which is equivalent to an intensity of $\sim 1 \times 10^7$ W/cm^2, lying within technologically available microwave sources [48]. The temporal full width at half maximum (t-FWHM) of the Gaussian envelope function $f(\tau)$ is chosen as $\Delta\tau_p = \tau_f \Big/ \left(5\sqrt{\ln 4}\right) \approx 0.17 \times \tau_f$, corresponding to a spectral full width at the half maxim (s-FWHM) $\Delta\omega_p \approx 0.44 \times 2\pi/\Delta\tau_p \approx 2.59 \times 2\pi/\tau_f$. Here, the t-FWHM $\Delta\tau_p$ is partiuclarly chosen such that the Gaussian envelope function $f(\tau)$ quickly falls off to near zero at $\tau = 0$ and $\tau = \tau_f$.

To attain good convergence, different pulse lengths and carrier frequencies may be chosen for orientation and entanglement control simulations. Here, the pulse length τ_f is chosen to be $\tau_f = 50$ (i.e., the pulse length $t_f \equiv \tau_f/B \approx 1305$ ps and the t-FWHM is $\Delta t_p = \Delta\tau_p/B \approx 222$ ps) at all rotor-to-rotor separations, i.e., $R = 1$ nm, 2 nm, 5 nm, 10 nm, and 50 nm in all orientation control simulations, whereas $\tau_f = 50$, 100, and 150, respectively, at the separations $R = 1$ nm, 3 nm, and 5 nm in entanglement control simulations. These latter pulse lengths give rise to the t-FWHM $\Delta\tau_p \approx 8.5$, 16.10, and 25.5, corresponding to the narrow s-FWHM values $\Delta\omega_p \approx 0.325$, 0.163, and 0.082, respectively.

In addition, the dipole operators $\mu\cos\varphi_1 = \mu\cos(-\varphi_1)$ and $\mu\cos\varphi_2 = \mu\cos(-\varphi_2)$ in Eq. (1), being even functions of φ_1 and φ_2, can only couple states of like symmetry (i.e., the state functions that are either both even, or both odd, functions of individual rotor angles). As a result, the initial states need to possess the same symmetry as the respective control objectives, Eqs. (18) and (24). For example, for a successful orientation control simulation for the perpendicular configuration $\theta = \pi/2$ and at the zero target angle $\alpha = 0$, only the state that is an even function of rotor angles, including the ground state $|E_1\rangle$ of the coupled rotors and the ground product state $|0\rangle \otimes |0\rangle$ of uncoupled rotors, can be considered as the initial state, since the corresponding dipole-dipole coupling $\widetilde{W}_{12}$ and orientation operator $\cos\varphi_1 + \cos\varphi_2$ are all even function of φ_1 and φ_2, see Eqs. (42) and (43). Similarly, for a successful entanglement control simulation, the initial state also needs to be an even function of φ_1 and φ_2 since the desired MES $|\psi_{\rm MES}\rangle$ is an even function of rotor angles, see Eq. (44) below.

Finally, we remark that the evolution of the wave function $|\psi(\tau)\rangle$ of the coupled rotors, cf. Eq. (8), is effectively driven by the dimensionless dipole-control field interaction $\widetilde{V}(\tau) \sim (\mu/B)\times\varepsilon(\tau)$, Eq. (6), which is proportional to the ratio μ/B. As a result, physically distinct pairs of rotors (not simulated in this paper) may experience the same effective dipole-field interaction $\widetilde{V}(\tau)$, despite their different dipole moments and rotational constants [49, 50].

A. Optimal orientation control

Here simulations have been carried out to find optimal control fields that concurrently orient both rotors toward the same target angle α. Specifically, we seek optimal control fields that maximize the joint orientation objective functional

$$J_O\left(t_f,\alpha\right) = \left\langle\psi\left(\tau_f\right)\right| \left[\cos\left(\varphi_1+\alpha\right)+\cos\left(\varphi_2+\alpha\right)\right] \left|\psi\left(\tau_f\right)\right\rangle, \tag{38}$$

for different configuration angles θ and target angles α. The main goal is to understand how the optimization of $J_O(\tau_f,\alpha)$ depends on the configuration angle θ and the target angle α at different separations between the two rotors. We recall that the dipole-dipole coupling strength between the two rotors at a fixed separation R is determined by the Γ value (i.e., see Eq.(5)).

First we present the strong dipole-dipole coupling case, $\Gamma = 12.46$, at the separation $R = 1$ nm, starting from the ground state $|E_1\rangle$ of the field-free coupled-rotor Hamiltonian H_0 in Eq. (2), i.e., $|\psi(0)\rangle = |E_1\rangle$. The initial control field $\varepsilon(0,\tau)$, Eqs. (35) - (37), is composed of three frequen-

cies $\omega_1 = 8.1248$, $\omega_2 = 7.5543$, and $\omega_3 = 6.8751$, corresponding to the sequential transitions $|E_1\rangle \rightarrow |E_7\rangle \rightarrow |E_{14}\rangle \rightarrow |E_{27}\rangle$ between four lowest dipole connected energy eigenstates of the coupled rotors at $R = 1$ nm. Fig. 2 shows the orientation optimal control results, respectively, for two configuration angles: (a) $\theta = \pi/4$ (an oblique configuration) and (b) $\theta = \pi/2$ (the perpendicular configuration). For the oblique configuration $\theta = \pi/4$, Fig. 2(a), it was found that the objective functional $J_O\left(\tau_f, \alpha\right)$ first increases quickly and eventually converges to the near global maximum value $\lambda_{\max} = 1.97$ for both target angles $\alpha = 0$ and $\alpha = \pi/3$. We remark that optimal control fields were always able to steer from the ground state $|E_1\rangle$ to the corresponding MOS, $|\psi_{\text{MOS}}\rangle$, whenever the inter-rotor axial vector $\mathbf{R}$ is at an oblique angle with respect to the $\hat{\mathbf{x}}$-axis, i.e., the configuration angle $\theta \neq \pi/2$, regardless of the target angle α (see further discussions below). We have also successfully performed simulations using different initial fields, including ones with much wider spectral bandwidths (i.e., containing many more than just three frequency components), confirming much slower convergence for the oblique configuration angles, when compared with the perpendicular one, as seen in Fig. 2(a) vs Fig. 2(b).

The case of the perpendicular configuration $\theta = \pi/2$ deserves a special attention. To facilitate the analysis, we recast Eq. (38) as

$$J_O\left(\tau_f, \alpha\right) = \cos\alpha \times J_C\left(\tau_f\right) - \sin\alpha \times J_S\left(\tau_f\right), \tag{39}$$

where

$$J_C\left(\tau_f\right) = \left\langle \psi\left(\tau_f\right)\right| \left(\cos\varphi_1 + \cos\varphi_2\right) \left|\psi\left(\tau_f\right)\right\rangle$$

and

$$J_S\left(\tau_f\right) = \left\langle \psi\left(\tau_f\right)\right| \left(\sin\varphi_1 + \sin\varphi_2\right) \left|\psi\left(\tau_f\right)\right\rangle.$$

It can be shown analytically that $J_S(\tau_f) = 0$ when the ground state $|E_1\rangle$ is chosen as the initial state $|\psi(0)\rangle$. In this case, both projections of the initial state wave function $|E_1\rangle$ and the final state wave function $|\psi\left(\tau_f\right)\rangle$ on to φ_1, φ_2 are symmetric functions of φ_1 and φ_2, i.e., $\langle -\varphi_1, -\varphi_2 | E_1\rangle = \langle \varphi_1, \varphi_2 | E_1\rangle$ and $\langle -\varphi_1, -\varphi_2 | \psi\left(\tau_f\right)\rangle = \langle \varphi_1, \varphi_2 | \psi\left(\tau_f\right)\rangle$, which implies $J_S(\tau_f) = 0$, noting that $\sin(-\varphi_1) + \sin(-\varphi_2) = -(\sin\varphi_1 + \sin\varphi_2)$. Consequently, the objective functional $J_O\left(\tau_f, \alpha\right)$ can be written as the product

$$J_O\left(\tau_f, \alpha\right) = \cos\alpha \times J_C(\tau_f), \tag{40}$$

which is bounded by the maximum value $\lambda_{\text{MOS}} \times \cos\alpha = 1.97 \times \cos\alpha$ (for $M = 8$). Accordingly, the gradient of the objective function needed to integrate the D-MORPH equation for the

perpendicular configuration angle $\theta = \pi/2$, can be written as

$$\frac{\delta J_O\left(\tau_f, \alpha\right)}{\delta\varepsilon\left(\tau\right)} = \cos\alpha \times \frac{\delta J_C\left(\tau_f\right)}{\delta\varepsilon\left(\tau\right)}, \tag{41}$$

which has a multiplication factor of $\cos\alpha$. The analysis leading to Eqs. (40) and (41) was numerically demonstrated in Fig. 2(b), showing that $J_O\left(\tau_f, \alpha\right)$ converges to the maximally allowed value of 1.97 at the target angle $\alpha = 0$ (black curve), while $J_O\left(\tau_f, \alpha\right)$ can only reach 0.985 for the target angle $\alpha = \pi/3$ (red curve), cf, Eq. (40). In the remaining discussions, we will only consider the $\alpha = 0$ target angle cases, since the simulations showed that all optimal control dynamical behavior is qualitatively the same at different target angles.

At the zero target angle, $\alpha = 0$, it is easy to see that the expectation value of the underlying orientation operator $\left\langle\varphi_1, \varphi_2\left|\hat{O}(\alpha = 0)\right|\varphi_1, \varphi_2\right\rangle$, cf. Eq. (17), is an even functions of rotor angles φ_1, φ_2. In particular, for the case of the perpendicular configuration, $\theta = \pi/2$, the two coupled rotors are indistinguishable with respect to the polarization (along the $\hat{\mathbf{x}}$-axis) of the control field, see Fig. 1, since the dipole-dipole interaction in Eq. (5)

$$\widetilde{W}_{12}(R, \theta = \pi/2, \varphi_1, \varphi_2) = \Gamma\left\{\cos\varphi_1\cos\varphi_2 - 2\sin\varphi_1\sin\varphi_2\right\}, \tag{42}$$

is symmetric with respect to the $\hat{\mathbf{x}}$-axis, i.e.,

$$\widetilde{W}_{12}(R, \theta = \pi/2, -\varphi_1, -\varphi_2) = W_{12}(R, \theta = \pi/2, \varphi_1, \varphi_2). \tag{43}$$

As a result, for optimal orientation control simulations of the coupled rotors, the initial state wave function $\langle\varphi_1, \varphi_2|\psi(0)\rangle$ must be an even function of the rotor angles φ_1 and φ_2 to enable successful optimal orientation controls when $\theta = \pi/2$ and $\alpha = 0$.

Figs. 3 and 4 show optimal control results, with $|E_1\rangle$ as the initial state, at the rotor-to-rotor separation $R = 1$ nm for two different configuration angles: $\theta = \pi/4$ in Fig. 3 and $\theta = \pi/2$ in Figs. 4. Each figure contains three panels, respectively, depicting (a) the temporal orientation evolution of rotor 1(note that two rotors are identical and possess the same temporal behavior), (b) the optimal control field and (c) the corresponding power spectrum. It was found that for both configuration angles $\theta = \pi/4$ in Fig. 3(a) and $\theta = \pi/2$ in Figs. 4(a), both expectation values of orientation show fast beating, due to transitions between the energy levels of the coupled rotors, and attain the desired numerical maximum 0.985 is attained at the terminal time τ_f. The intensities, $\sim 2.46\times10^7$ W/cm^2 and $\sim 1.81\times10^7$ W/cm^2, respectively, of two optimal control fields in Figs. 3(b) and 4(b) are slightly larger than $\sim 1\times10^7$ W/cm^2 for the initial field, cf. Eqs. (35) - (37). The

corresponding power spectra in Figs. 3(c) and 4(c) resemble each other, containing many small peaks, a small d.c. component, and three tall, but narrow, peaks over a wide spectral window from $\omega = 0$ to $\omega = 40$; the three main peaks (labeled as 1, 2, 3) have relative heights approximately of the ratio 5:3:2, which coincide with the same three frequencies comprising of the initial field. The slight increases of three initial peaks along with numerous much smaller new peaks of the power spectra of optimal fields are responsible for optimal constructive quantum interference enabling the coupled rotors to reach the desired MOS $|\psi_{\rm MOS}\rangle$ of the coupled rotors.

Naturally, we expect convergence to the desired MOS, regardless of the initial field or state (i.e provided it has the proper symmetry) due to control landscape expected to be free of traps. Furthermore, below we confirm this expectation with further simulations. For comparison, we have performed three additional simulations for $\alpha = 0$ at the $R = 1$ nm: (A1) The oblique configuration $\theta = \pi/4$ starting from the ground state $|E_1\rangle$, with the initial field frequencies $\omega_1 = 2$, $\omega_2 = 6$, and $\omega_3 = 10$, corresponding to the sequential transitions $|0\rangle \otimes |0\rangle \rightarrow |1\rangle \otimes |1\rangle \rightarrow |2\rangle \otimes |2\rangle \rightarrow |3\rangle \otimes |3\rangle$, between the product states of the uncoupled rotors. (A2) The perpendicular configuration $\theta = \pi/2$, starting from the ground state $|E_1\rangle$, with the same initial field frequencies $\omega_1 = 2$, $\omega_2 = 6$, and $\omega_3 = 10$ as in (A1). (A3) The perpendicular configuration $\theta = \pi/2$, starting from the product state $|0\rangle\otimes|0\rangle$ of uncoupled rotors, with the same three initial field frequencies $\omega_1 = 8.1248$, $\omega_2 = 7.5543$, and $\omega_3 = 6.8751$ used in Figs. 2 - 4. Simulation (A1) produced a similar strong modulated beat pattern in the time evolution of optimal orientation (not shown) to that seen in Fig. 3(a), despite having a very different optimal field (not shown) from that in Fig. 3(b).

For the perpendicular configuration $\theta = \pi/2$, it was found that the results from the simulation (A2), Fig. 5, and the simulation (A3), Fig. 6, are quite different from each other, due to distinct initial fields and different initial states, and from those in Fig. 4, respectively. These latter additional simulations (A2) and (A3) exhibit very different fast beating patterns in the evolution of orientation (i.e., compare Figs. 4(a) versus that of Figs. 5(a) and 6(a)). In particular, there is no discernible rotational modulation appearing in the very early time at $\tau < \tau_{\rm rot} = 2\pi$ in Figs. 5(a) and 6(a), in sharp contrast to those found in Fig. 4(a). As expected, there are also distinct differences in the optimal control fields, of Figs. 4(b), 5(b) and Fig. 6(b). In Sec. III C, similar qualitative distinction were also found for the optimal control transition from a much more complex initial state $|\psi_{\rm MES}\rangle$, Eq. (24), to the final state $|\psi_{\rm MOS}\rangle$, see Fig. 14(d). Collectively, these numerical simulations show that the key optimal control principles in general do not depend on different choices of the initial state or control field, although detailed dynamical distinctions are evident.

The extensive numerical simulations discussed above for the strongly dipole-dipole coupled rotors at $R = 1$ nm showed that the optimally reachable M-dependent orientation (and entanglement later in Sec. III B), with nanosecond GHz pulses (of the pulse length ~ 1.305 ns), are very close to their respective upper bounds that can be reached by arbitrarily long pulses. The intensity of the resultant optimal control fields in these simulations, ranging from $\sim 2 \times 10^7$ W/cm^2 to $\sim 4 \times 10^7$ W/cm^2, are of the same order of magnitude as the intensity of the presently available high-power microwave sources [48]. Moreover, many existing OCT simulations [51] show that weaker and longer optimal control pulses can be effective. Accordingly, we performed additional simulations (results not shown) to generate much weaker optimal fields by considering much weaker initial fields, of the intensity $\sim 1 \times 10^3$ W/cm^2 for pulse lengths up to $t_f = 60$ ns, but they were considerably more expensive computationally.

We now present the optimal control simulations for the intermediate dipole-dipole coupling case, $\Gamma = 1.55$, at the separation $R = 2$ nm and the weak dipole-dipole coupling case, $\Gamma = 0.1$, at the separation $R = 5$ nm; for both cases, the configuration angle is $\theta = \pi/2$ and the initial state is $|E_1\rangle$ of the coupled rotors at their respective separations. The initial field $\varepsilon(0, \tau)$ is composed of three frequencies: at $R = 2$ nm, $\omega_1 = 2.2475$, $\omega_2 = 3.5415$, and $\omega_3 = 4.6245$, corresponding to the sequential transitions $|E_1\rangle \rightarrow |E_6\rangle \rightarrow |E_{17}\rangle \rightarrow |E_{28}\rangle$ between four lowest dipole connected energy eigenstates of the coupled rotors, and at $R = 5$ nm, $\omega_1 = 1$, $\omega_2 = 3$, and $\omega_3 = 5$, corresponding to the sequential transitions $|0\rangle \rightarrow |1\rangle \rightarrow 2\rangle \rightarrow |3\rangle$ of a single rotor. Fig. 7 shows the optimal control orientation dynamics for rotor 1 (the behavior of rotor 2 is identical to that of rotor 1) at separations $R = 2$ nm and $R = 5$ nm. It was found that at the intermediate separation $R = 2$ nm, the temporal behavior of the orientation driven by the optimal control field, Fig. 7(a), is significantly different from that of the uncoupled rotors driven by the same control field, Fig. 7(b). In contrast, at the large separation $R = 5$ nm, the temporal behavior of orientation, Fig. 7(c), is virtually the same as that of the uncoupled rotors in Fig. 7(d), as expected. Furthermore, the result in Fig. 7(c) is naturally also very different from the strongly coupled rotors in Figs. 3 - 6. Related behavior is also evident in Fig. 8 showing the field-free evolution after attaining the MOS: no tangible revival behavior appears for the intermediate coupling case at $R = 2$ nm, Fig. 8(a), but very clear revival peaks are presented for the weak coupling case at $R = 5$ nm, Fig. 8(b), beginning to resemble those of a free rotor, Fig. 8(c).

Finally, we present the very weak dipole-dipole coupling case, $\Gamma = 1.24 \times 10^{-2}$, at the separation $R = 10$ nm and the extremely weak dipole-dipole coupling case, $\Gamma = 9.97 \times 10^{-5}$, at the

separation $R = 50$ nm for the configuration angle $\theta = \frac{\pi}{2}$, starting from the ground state $|E_1\rangle$ of the coupled rotors at the respective separations. Figs. 9 (a) and (b) show the optimal control orientation dynamics of rotor 1, as a function of time τ, at two separations $R = 10$ nm and $R = 50$ nm, respectively. The initial field $\varepsilon(0, \tau)$ is composed of three frequencies: $\omega_1 = 1$, $\omega_2 = 3$, and $\omega_3 = 5$, corresponding to the sequential transitions $|0\rangle \rightarrow |1\rangle \rightarrow 2\rangle \rightarrow |3\rangle$ of a single rotor. The optimal fields (not shown) were virtually identical, consistent with the near free rotor behavior of both cases. It was found that the temporal behavior of orientation in the presence of optimal control fields are virtually the same for both cases over short time, out to $\tau_f = 50$. In contrast, Fig. 10 shows the long time field-free evolution of orientation dynamics of rotor 1, after turning off the optimal control field, at either $R = 10$ nm, Fig. 10(a), or $R = 50$ nm, Fig. 10(b). It was also found that in addition to the highly oscillatory beats reminiscence of the quick rotation of the free rotor, cf. Fig.8(c), the temporal evolution of the field-free orientation of the coupled rotors at these large separations exhibits a strikingly unique long-time revival pattern revealed by the envelopes of the blackened large lobes that arise from slow modulation of the much faster, *nearly* free rotation.

The long time revival patterns in Fig. 10 can be understood in terms of the small energy splittings of degenerate free-rotor product states due to the perturbation brought about by the dipole-dipole interaction. It is shown in Appendix C that (i) the two-fold degenerate free-rotor product states $|m, m+1\rangle$ and $|m+1, m\rangle$ are split into two sublevels, respectively, with energy shifts $-\Gamma/4$ and $\Gamma/4$, (ii) the two-fold degenerate free-rotor product states $|m, -(m+1)\rangle$ and $|m+1, -m\rangle$ are split into two sublevels, respectively, with energy shifts $-3\Gamma/4$ and $3\Gamma/4$, and (iii) the four-fold degenerate free-rotor product states $|0, 1\rangle, |1, 0\rangle, |0, -1\rangle$ and $|-1, 0\rangle$ are split into four sublevels, respectively, with energy shifts $-\Gamma, -\Gamma/2$, $\Gamma/2$, and Γ. Moreover, it is shown in Appendix D that the dipole-like orientation operator only links the dipole-dipole perturbed degenerate free-rotor product states to the unperturbed ones. As a result, there are four likely long-time overlapping revival patterns, corresponding to the periods $T_L, T_L/2, T_L/3$ and $T_L/4$, with $T_L \equiv T_L(R) = 4\tau_{\rm rot}/\Gamma = 8\pi/\Gamma$, evident at very large values of R. The longest revival periods $T_L(R)$, Eq. (D16), which corresponds to the time interval between the largest two consecutive lobes, are $T_L(10) = 8\pi/\Gamma \approx 2000$ for R = 10 nm, Fig. 10(a), and $T_L(50) = 8\pi/\Gamma \approx 2.5 \times 10^5$ for R = 50 nm, Fig. 10(b), yielding a ratio of $T_L(10)/T_L(50) = 1/125$, which is in agreement with the relative recurrence times of the largest lobes. The other shorter revival periods, $T_L/2, T_L/3$ and $T_L/4$, each an integer fraction of T_L, are responsible for additional lobes of smaller heights between the largest lobes in Figs. 10. We remark that these long-time revival patterns are completely

absent for free rotors in the limit $R = \infty$.

B. Optimal control and field-free transport of entanglement

Here we present the optimal control simulations for creating the MES $|\psi_{\rm MES}\rangle$, Eq. (24), of the two rotors fixed at three different separations $R = 1$ nm, 3 nm and 5 nm for the configuration angle $\theta = \pi/2$, starting from the ground state $|E_1\rangle$ of the coupled rotors at the respective separations. It is noted that in the absence of the external field, the coupled rotors are modestly entangled due to their mutual dipole-dipole coupling, for example, the two-rotor ground-state entanglement entropies $S_{\rm vN}(|E_1\rangle)$ (for $M = 8$) are 0.81, 0.25, and 0.02 at these three separations, respectively. Moreover, it can be shown that the function $\langle\varphi_1, \varphi_2\,|\psi_{\rm MES}\rangle$ is an even function of the rotor angles φ_1 and φ_2, i.e.,

$$\langle\varphi_1, \varphi_2\,|\psi_{\rm MES}\rangle = \langle -\varphi_1, -\varphi_2\,|\psi_{\rm MES}\rangle\,, \tag{44}$$

cf. Eq. (24). In the following calculations to create the MES $|\psi_{\rm MES}\rangle$, the ground state $|E_1\rangle$ is chosen as the initial state and the optimal control field is found by maximizing the MES objective functional

$$J_E(\tau_f) = \langle\psi(\tau_f)|\psi_{\rm MES}\rangle\langle\psi_{\rm MES}|\psi(\tau_f)\rangle. \tag{45}$$

Here three different pulse lengths τ_f= 50 for $R = 1$ nm, τ_f= 100 for $R = 3$ nm and τ_f= 150 for $R = 5$ nm of the control field were adopted, since it requires more effort to attain the maximal entanglement at larger separations due to the rapidly decreasing dipole-dipole coupling between the two rotors.

Figure 11 depicts time evolution of the entanglement entropy $S_{\rm vN}(|\psi(\tau)\rangle)$ at $R = 1$ nm, Fig. 11(a), $R = 3$ nm, Fig. 11(b), and $R = 5$ nm, Fig. 11(c), in the presence of (1) the initial field (red curve), (2) the optimal field (blue curve), and (3) the zero field (black curve). It was found that the value of optimal field driven entropy (blue curves), after remaining virtually unchanged in the initial transient period, quickly rises up to reach the expected maximal entanglement value, $S_{\rm vN}\,(|\psi_{\rm MES}\rangle) = \ln 17 \approx 2.8332$, at all three separations; as expected, it took more control iterations to obtain optimal fields at larger separations, despite using longer control pulses. Naturally, in the limit of $R \to \infty$, the dipole-dipole interaction $\widetilde{W}_{12}(R) \to 0$, and two rotors cease to be entangled with or without any electric field, which only address individual rotors, cf. Eq. (1). For these optimal control simulations, as well as those in Sec. III C, the constituent frequencies

for the initial field $\varepsilon(0,\tau)$ are : $\omega_1 = 2, \omega_2 = 6, \omega_3 = 10$ (in units of B), which, respectively, correspond to the first three transition frequencies $|00\rangle \rightarrow |11\rangle \rightarrow |22\rangle \rightarrow |33\rangle$, among all product states $|m_1 = m\rangle \otimes |m_2 = m\rangle$, $m = -M, \cdots, -1, 0, 1, \cdots, +M$, that form the desired MES of the coupled rotors, cf. Eq. (24).

Figures 12(a) and 12(b), respectively, show the optimal control field (with an intensity equal to $\sim 3.6 \times 10^7$ W/cm^2) and the corresponding power spectrum for the entanglement control simulations at the rotor-to-rotor separation $R = 1$ nm. It was found that when comparing the results from the orientation control simulations for $\theta = \pi/2$ and $\alpha = 0$ at the $R = 1$ nm, starting from the same ground state $|E_1\rangle$ and the same initial field, the strong beating pattern of the resultant optimal control field in Fig. 12(a) qualitatively resembles its counterpart in Fig. 5(b) despite the large difference in the control objectives, i.e., entanglement, Fig. 11(a) vs orientation, Fig. 5(a). The effect of this difference in control objectives can be clearly seen in the respective power spectra in Fig. 5(c) and Fig. 12(b), as manifested in several more visible small peaks in Fig. 12(b) besides the three dominant peaks at $\omega_1 = 2, \omega_2 = 6, \omega_3 = 10$ (labeled as 1, 2, 3) associated with the three frequency components in the initial field.

We also show the field-free evolution of the entropy for the MES as the two rotors are moved away from each other at various speeds, including both in the adiabatic limit (i.e., slow separation) and in the sudden limit (i.e., rapid separation). Specifically, we have solved the corresponding time-dependent coupled equation, Eq. (8), with a time-dependent parameter $R(\tau)$ in the dipole-dipole interaction $\widetilde{W}_{12}$, Eq. (5), *after* the optimal control was terminated. Fig. 13 shows the field-free evolution of the entanglement entropy by allowing the separation R to change at different rates according to the linear relation

$$R(\tau) = R_0 + k\tau, \tag{46}$$

where $R_0 = 1$ nm, $k = 0.01, 0.1, 1, 10$ and 100. Starting with the maximal value $S_{\rm vN}(|\psi_{\rm MES}\rangle) \approx 2.8332$, it was found that (1) for $k = 0.01$ the value of entropy oscillates rapidly at small separations and converges to 2.4188 at the large separation, Fig. 13(a), (2) for $k = 0.1$ the value of entropy oscillates moderately at small separations and eventually converges to 2.3219, Fig. 13(b), (3) for $k = 1$ the value of entropy drops to about 2.4 suddenly at small separations and converges to 2.5507, Fig. 13(c), (4) for $k = 10$ the value of entropy at first falls off with a gentle modulation and converges to 2.8204, Fig. 13(d), and finally (5) for $k = 100$ the value of entropy simply falls off smoothly and converges to 2.8331 (i.e., it changes very little from its initial value), Nonetheless, Fig. 13(e). Figs. 11 and 13 demonstrated not only that the MES can be easily obtained

using an optimally tailored control field at separations when the dipole-dipole coupling between two rotors is sufficiently large, but the resultant maximal entanglement entropy remains basically unchanged where the two rotors are moved apart in the sudden limit (corresponding to $k = 100$), and drops only moderately in the adiabatic limit (corresponding to $k = 0.01$), regardless the speed of separation.

C. Optimal control transition dynamics between the MOS and the MES

Here we present the interplay of optimal control transition dynamics between the MOS and MES of the coupled rotors for the perpendicular configuration angle $\theta = \pi/2$ in the strong dipole-dipole interaction limit at separation $R = 1$ nm. Specifically, we have performed optimal control simulations for the transition $|\psi_{\rm MES}\rangle \rightarrow |\psi_{\rm MOS}\rangle$ and for the transition $|\psi_{\rm MOS}\rangle \rightarrow |\psi_{\rm MES}\rangle$. In both optimal control simulations, we used the same initial field (i.e., composed of three frequency components $\omega_1 = 2, \omega_2 = 6, \omega_3 = 10$, in units of B) as in Sec. III B.

Figure 14 shows the optimal control transition dynamics for $|\psi_{\rm MES}\rangle \rightarrow |\psi_{\rm MOS}\rangle$. In this case, an optimal control field is obtained under the circumstance that two rotors initially possess a zero orientation expectation value and are coupled via a very strong dipole-dipole interaction $R = 1$ nm. Specifically, the time evolution of the entanglement entropy $S_{\rm vN}(|\psi(\tau)\rangle)$, and that of the expectation value of orientation $\left\langle \hat{O}_1(\tau) \right\rangle = \langle\psi(\tau)|\cos\varphi_1|\psi(\tau)\rangle$ are shown for both initial and optimal fields. We note that initially $S_{\rm vN}(|\psi(0)\rangle) \approx 2.8332$ and $\left\langle \hat{O}_1(0) \right\rangle = 0$. It was found that (1) with the initial field, the entropy first decreases to ~ 1.5 at the midpoint of the pulse length, then rises up to just below 2 at the terminal time τ_f, Fig. 14(a), and (2) with the optimal field, the entropy slowly reduces and then rapidly plunges to zero at the terminal time τ_f, Fig. 14(b). On the other hand, we find that, (3) in the presence of the initial field, the expectation value of the orientation $J_O(\tau)$ oscillates modestly around the zero value throughout the evolution, Fig. 14(c), and (4) with the optimal field, it oscillates modestly until a sudden jump to the optimal target value of 0.985 (for one rotor) at the very end of the control pulse, Fig. 14(d). In the absence of any field, the expectation value of the orientation (not shown) remains at the zero value throughout, see Appendix B. Also, it was found that the resultant optimal field and power spectrum (not shown) qualitatively resemble those shown in Fig. 5(b) and 5(c), despite the large difference in the initial states, i.e., $|\psi_{\rm MES}\rangle$ vs. $|0\rangle \otimes |0\rangle$.

Figure 15 shows the time evolution of entropy and orientation for optimal control transition

$|\psi_{\rm MOS}\rangle \rightarrow |\psi_{\rm MES}\rangle$, which is the opposite of the optimal control transition in Fig. 14. For this optimal control process, $S_{\rm vN}(|\psi(0)\rangle) = 0$ and $\left\langle \hat{O}_1(0) \right\rangle = 0.985$. It was found that (1) the entropy remains just above 1 throughout when the initial field was on, Fig. 15(a), (2) the entropy first increases gradually, then jumps suddenly to its optimal value of 2.83 at the terminal time τ_f when the optimal field was on, Fig. 15(b), and (3) the expectation value of orientation $\left\langle \hat{O}_1(\tau) \right\rangle$ drops rapidly with either the initial or optimal fields, and then oscillates only modestly with an almost zero amplitude throughout, Figs. 15(c) and (d). As expected, the corresponding expectation value $\left\langle \hat{O}_1(\tau) \right\rangle$ becomes zero when the optimal control field reaches $\tau_f = 50$, Fig. 15(d). Finally, it was found that the resultant optimal field and power spectrum (not shown) resemble those shown in Fig. 12(a) and 12(b), despite the large difference in the initial states, i.e., $|\psi_{\rm MOS}\rangle$ vs. $|0\rangle \otimes |0\rangle$.

IV. CONCLUSION

We have performed optimal control simulations for maximizing orientation and entanglement of two coupled quantum rotors that lie in a plane at a wide range of fixed separations. The resultant optimal fields leading to maximal orientation and entanglement, respectively, are in the microwave [43, 52] range of the spectrum, corresponding the rotational transition spectra of the coupled rotors. It was found that the maximal orientation of the two rotors can be achieved regardless of the separation between the rotors. Of special interest is, at vary large separations, the orientation peak expectation value recurs with a very long period proportional to the cubic power of the separation R. The calculations showed that the optimal control dynamics are distinct at different separations. Moreover, it was shown that the maximally entangled state can be most efficiently created at sufficiently small separations. Importantly, it was observed that the maximally entangled state of the coupled rotors remained largely unchanged in the sudden limit when the rotors are quickly transported to large separations and only decreases moderately in the adiabatic limit when they slowly moved apart. Finally, optimal control simulations easily found fields to steer a maximally entangled state having a zero averaged orientation to a maximally orientated state having a zero entanglement and *vice versa*.

The optimal controlled dynamics studied in this paper, in principle, can be realized at the surface of appropriate solids [26]. Although the current work is limited to pure state optimal orientation/entanglement controlled dynamics of two identical planar polar molecules, much of results and analysis may be useful as a basis to understand the future studies of three or more identical ro-

tors. The same techniques can be extended to optimal orientation/entanglement control problems for non-identical rotors and for coupled rotors in thermal ensembles or mixed states.

ACKNOWLEDGEMENTS

T.-S.H. acknowledges support from the DOE Grant No. DE-FG02- 02ER15344, H.R. from the NSF Grant No. CHE- 1464569, and H. Yu was supported by China Scholarship Council.

APPENDIX A: MAXIMALLY ORIENTED STATES

Consider the eigenvalue problems for the $(2M+1)\times(2M+1)$ dimensional matrix representation of the orientation operators $\hat{O}_1(\alpha) \equiv \cos(\varphi_1 + \alpha)$ and $\hat{O}_2(\alpha) \equiv \cos(\varphi_2 + \alpha)$ given by the following eigenvalue equations:

$$\hat{O}_j(\alpha)\left|\lambda_k^{[j]}(\alpha)\right\rangle = \lambda_k^{[j]}\left|\lambda_k^{[j]}(\alpha)\right\rangle,\ k = 1, \cdots, 2M+1 \text{ and } j = 1, 2. \tag{A1}$$

It can be shown that the operator $\cos(\varphi_j + \alpha)$ for each rotor, here $j = 1, 2$, can be explicitly represented by a $(2M+1)\times(2M+1)$ dimensional Hermitian tridiagonal Toeplitz matrix

$$\cos(\varphi+\alpha) = \begin{pmatrix} 0 & \frac{1}{2}\exp(i\alpha) & 0 & 0 & \cdots & 0 & 0 \\ \frac{1}{2}\exp(-i\alpha) & 0 & \frac{1}{2}\exp(i\alpha) & 0 & \cdots & 0 & 0 \\ 0 & \frac{1}{2}\exp(-i\alpha) & 0 & \frac{1}{2}\exp(i\alpha) & \cdots & 0 & 0 \\ 0 & 0 & \frac{1}{2}\exp(-i\alpha) & 0 & \cdots & 0 & 0 \\ \vdots & \vdots & \vdots & \vdots & \ddots & \vdots & \vdots \\ 0 & 0 & 0 & 0 & \cdots & 0 & \frac{1}{2}\exp(i\alpha) \\ 0 & 0 & 0 & 0 & \cdots & \frac{1}{2}\exp(-i\alpha) & 0 \end{pmatrix}, \tag{A2}$$

which is known [53] to possess eigenvalues and eigenvectors in closed form, i.e.,

$$\lambda_k^{[j]} = \cos\left(\frac{k\pi}{(2M+2)}\right),\ k = 1, \cdots, 2M+1, \tag{A3}$$

and

$$\left|\lambda_k^{[j]}(\alpha)\right\rangle = \frac{1}{\sqrt{N_k}} \begin{pmatrix} \exp(iM\alpha) \times \sin\left(\frac{k\pi}{2M+2}\right) \\ \vdots \\ \exp(i\alpha) \times \sin\left(\frac{Mk\pi}{2M+2}\right) \\ \sin\left(\frac{(M+1)k\pi}{2M+2}\right) \\ \exp(-i\alpha) \times \sin\left(\frac{(M+2)k\pi}{2M+2}\right) \\ \vdots \\ \exp(-iM\alpha) \times \sin\left(\frac{(2M+1)k\pi}{2M+2}\right) \end{pmatrix}, \; k = 1, \cdots, 2M+1, \tag{A4}$$

where

$$\begin{aligned} N_k &\equiv \sum_{\ell=1}^{2M+1} \sin^2\left(\frac{\ell k\pi}{2M+2}\right) \\ &= \frac{1}{2}\sum_{\ell=1}^{2M+1}\left\{1 - \cos\left(\frac{\ell k\pi}{M+1}\right)\right\} \\ &= \frac{2M+1}{2} - \frac{1}{2}(-1)^k \frac{\sin\left((2M+1)\frac{k\pi}{2M+2}\right)}{\sin\left(\frac{k\pi}{2M+2}\right)} \end{aligned} \tag{A5}$$

is the normalization factor. Note that all eigenvalues $\lambda_k^{[j]}$, Eq. (A3), of the single rotor orientation operator $\cos(\varphi_i+\alpha)$ are independent of the target angle α, while the associated eigenstates $\left|\lambda_k^{[j]}(\alpha)\right\rangle$, Eq. (A4), are α-dependent.

Now, consider the eigenvalues and eigenvectors of the composite coupled-rotor orientation operator

$$\hat{O}(\alpha) = \hat{O}_1(\alpha) + \hat{O}_2(\alpha) = \cos(\varphi_1 + \alpha) + \cos(\varphi_2 + \alpha), \tag{A6}$$

defined in the Hilbert space spanned by $(2M+1)^2$ two-rotor product states $|m_1\rangle \otimes |m_2\rangle$, with $m_1, m_2 = -M, \cdots, -1, 0, +1, \cdots, M$. Since the composite operator $\hat{O}(\alpha)$ is a simple summation of individual single rotor operators $\hat{O}_1(\alpha)$ and $\hat{O}_2(\alpha)$, all of its eigenvectors can be written as the product states $\left|\lambda_{k_1}^{[1]}(\alpha)\right\rangle \otimes \left|\lambda_{k_2}^{[2]}(\alpha)\right\rangle$, respectively, associated with the eigenvalues

$$\lambda_{k_1}^{[1]} + \lambda_{k_2}^{[2]} = \cos\left(\frac{k_1\pi}{2M+2}\right) + \cos\left(\frac{k_2\pi}{2M+2}\right), \tag{A7}$$

satisfying the eigen-relations

$$\hat{O}(\alpha)\left\{\left|\lambda_{k_1}^{[1]}(\alpha)\right\rangle \otimes \left|\lambda_{k_2}^{[2]}(\alpha)\right\rangle\right\} = \left(\lambda_{k_1}^{[1]} + \lambda_{k_2}^{[2]}\right)\left\{\left|\lambda_{k_1}^{[1]}(\alpha)\right\rangle \otimes \left|\lambda_{k_2}^{[2]}(\alpha)\right\rangle\right\}, \tag{A8}$$

where $k_1, k_2 = 1, \cdots, M-1, M, M+1, \cdots, 2M+1$. By identifying

$$\left|\lambda_{\max}^{[1]}(\alpha)\right\rangle \equiv \left|\lambda_{k_1=1}^{[1]}\right\rangle \tag{A9}$$

and

$$\left|\lambda_{\max}^{[2]}(\alpha)\right\rangle \equiv \left|\lambda_{k_2=1}^{[2]}\right\rangle, \tag{A10}$$

respectively, as the maximally oriented eigenstates (for uncoupled single rotors) associated with the largest eigenvalues

$$\lambda_{\max}^{[1]} = \lambda_{k_1=1}^{[1]} = \cos\left(\frac{\pi}{2M+2}\right) \tag{A11}$$

and

$$\lambda_{\max}^{[2]} = \lambda_{k_2=1}^{[2]} = \cos\left(\frac{\pi}{2M+2}\right), \tag{A12}$$

we can obtain the maximal orientation (for coupled rotors)

$$\lambda_{\max} = \lambda_{\max}^{[1]} + \lambda_{\max}^{[2]} = 2\cos\left(\frac{\pi}{2M+2}\right) \tag{A13}$$

corresponding to the maximally oriented product eigenstate

$$|\lambda_{\max}(\alpha)\rangle = \left|\lambda_{\max}^{[1]}(\alpha)\right\rangle \otimes \left|\lambda_{\max}^{[2]}(\alpha)\right\rangle, \tag{A14}$$

where

$$\begin{aligned}\left|\lambda_{\max}^{[j]}(\alpha)\right\rangle &= \frac{1}{\sqrt{N_1}}\begin{pmatrix} \exp(iM\alpha)\times\cos\left(\frac{M\pi}{2M+2}\right) \\ \vdots \\ \exp(i\alpha)\times\cos\left(\frac{\pi}{2M+2}\right) \\ 1 \\ \exp(-i\alpha)\times\cos\left(\frac{\pi}{2M+2}\right) \\ \vdots \\ \exp(-iM\alpha)\times\cos\left(\frac{M\pi}{2M+2}\right)\end{pmatrix} \\ &= \frac{1}{\sqrt{N_1}}\left\{|0\rangle + \sum_{m_j=1}^{M}\cos\left(\frac{m_j\pi}{2M+2}\right)\times\left[\left|m_j\right\rangle e^{im_j\alpha} + \left|-m_j\right\rangle e^{-im_j\alpha}\right]\right\},\end{aligned} \tag{A15}$$

with $j = 1, 2$ and

$$N_1 = \frac{2M+1}{2} + \frac{1}{2}\frac{\sin\left((2M+1)\frac{\pi}{2M+2}\right)}{\sin\left(\frac{\pi}{2M+2}\right)}. \tag{A16}$$

By invoking Eqs. (15) and (A15), we immediately obtain

$$\left\langle\varphi_j\left|\lambda_{\max}^{[j]}(\alpha)\right\rangle\right. = \frac{1}{\sqrt{2N_1\pi}}\left\{1 + 2\sum_{m_j=1}^{M}\cos\left(\frac{m_j\pi}{2M+2}\right)\times\cos\left(m_j\left(\varphi_j+\alpha\right)\right)\right\}, \; j = 1, 2, \tag{A17}$$

which is an even function of the rotor angle $\varphi_j \in [-\pi, \pi]$ when $\alpha = 0$. As a result, we arrive at

$$\langle\varphi_1, \varphi_2\,|\lambda_{\max}(\alpha = 0)\rangle = \langle -\varphi_1, -\varphi_2\,|\lambda_{\max}(\alpha = 0)\rangle\,, \tag{A18}$$

which is an even function of both rotor angles φ_1 and φ_2.

APPENDIX B: ZERO EXPECTATION VALUE OF ORIENTATION FOR MAXIMALLY ENTANGLED STATES - PROOF OF EQ. (28)

The canonical maximally entangled state of two coupled identical planar rotors is given as [41]

$$|\psi_{\rm MES}\rangle = \frac{1}{\sqrt{2M+1}} \sum_{m=-M}^{M} |m_1 = m\rangle \otimes |m_2 = m\rangle \,. \tag{B1}$$

The corresponding field-free Hamiltonian $\widetilde{H}_0$, Eq. (2), is separable in the coordinates $\xi_1 = (\varphi_1 + \varphi_2)/2$ and $\xi_2 = (\varphi_1 - \varphi_2)/2$, i.e.,

$$\widetilde{H}_0 = \widetilde{H}_{\xi_1} + \widetilde{H}_{\xi_2}, \tag{B2}$$

where

$$\widetilde{H}_{\xi_1} = -\frac{1}{2}\frac{\partial^2}{\partial \xi_1^2} + \frac{3\Gamma}{2}\left[\left(1 - 2\cos^2\theta\right)\cos\left(2\xi_1\right) - \sin\left(2\theta\right)\sin\left(2\xi_1\right)\right] \tag{B3}$$

and

$$\widetilde{H}_{\xi_2} = -\frac{1}{2}\frac{\partial^2}{\partial \xi_2^2} - \frac{\Gamma\cos 2\xi_2}{2}. \tag{B4}$$

The separation indices 1 and 2 may be exchanged due to the identical nature of the rotors. The canonical maximally entangled state $|\psi_{\rm MES}\rangle$ in Eq. (B1) can be projected on to φ_1 , φ_2, resulting in the relation

$$\begin{aligned}
\langle \varphi_1, \varphi_2 | \psi_{\rm MES}\rangle &= \frac{1}{\sqrt{2M+1}} \sum_{m=-M}^{M} \langle \varphi_1 | m_1 = m\rangle \langle \varphi_2 | m_2 = m\rangle \\
&= \frac{1}{2\pi\sqrt{2M+1}} \sum_{m=-M}^{M} \exp\left[im\left(\varphi_1 + \varphi_2\right)\right] \\
&= \frac{1}{\pi\sqrt{2M+1}} \sum_{m=1}^{M} \left\{\frac{1}{2} + \cos\left[m\left(\varphi_1 + \varphi_2\right)\right]\right\} \qquad \text{(B5)} \\
&= \frac{1}{\pi\sqrt{2M+1}} \sum_{m=1}^{M} \left\{\frac{1}{2} + \cos\left(2m\xi_1\right)\right\} \\
&= \langle \xi_1 | \psi_{\rm MES}\rangle, \qquad \text{(B6)}
\end{aligned}$$

which only depends on the new angular variable ξ_1, but not ξ_2. From Eq. (B2), the free-evolution propagator associated with $\widetilde{H}_0$ can be written as

$$U_0\left(\tau, 0\right) = U_{\xi_1}\left(\tau, 0\right) U_{\xi_2}\left(\tau, 0\right), \tag{B7}$$

where

$$U_{\xi_1}\left(\tau, 0\right) = \exp\left(-i\widetilde{H}_{\xi_1}\tau\right) \tag{B8}$$

and

$$U_{\xi_2}(\tau,0)=\exp\left(-i\widetilde{H}_{\xi_2}\tau\right). \tag{B9}$$

As a result, the free evolution of the canonical maximally entangled state can be expressed as

$$\langle\xi_1|\psi_{\rm MES}(\tau)\rangle=\langle\xi_1|\,U_{\xi_1}(\tau,0)\,|\psi_{\rm MES}(0)\rangle\,,\;\;|\psi_{\rm MES}(0)\rangle=|\psi_{\rm MES}\rangle\,. \tag{B10}$$

In addition, the orientation operator of the two identical planar rotors can be recast as

$$\hat{O}(\alpha)\equiv\cos(\varphi_1+\alpha)+\cos(\varphi_2+\alpha)=2\cos(\xi_1+\alpha)\cos\xi_2, \tag{B11}$$

noting that $\varphi_1=\xi_1+\xi_2$ and $\varphi_2=\xi_1-\xi_2$. From Eqs. (B10) and (B11), we find that, in the absence of the control field, the free evolution of the expectation value of the orientation operator associated with the canonical maximally entangled state of the two identical polar planar rotors can be simply computed as follows:

$$\begin{aligned}
&\langle\psi_{\rm MES}(\tau)|\cos(\varphi_1+\alpha)+\cos(\varphi_2+\alpha)\,|\psi_{\rm MES}(\tau)\rangle\\
&=\int_0^{2\pi}d\varphi_1\int_0^{2\pi}d\varphi_2\langle\psi_{\rm MES}(\tau)\,|\varphi_1,\varphi_2\rangle\left[\cos(\varphi_1+\alpha)+\cos(\varphi_2+\alpha)\right]\\
&\times\langle\varphi_1,\varphi_2|\psi_{\rm MES}(\tau)\rangle\\
&=2\int_0^{2\pi}d\xi_1\int_{-\pi}^{\pi}d\xi_2\langle\psi_{\rm MES}(\tau)\,|\xi_1\rangle\cos(\xi_1+\alpha)\cos\xi_2\langle\xi_1|\psi_{\rm MES}(\tau)\rangle\\
&=2\,\langle\psi_{\rm MES}(\tau)|\cos(\xi_1+\alpha)\,|\psi_{\rm MES}(\tau)\rangle\int_{-\pi}^{\pi}d\xi_2\cos\xi_2\\
&=0\;\;\forall\tau\geq0.
\end{aligned} \tag{B12}$$

APPENDIX C: PERTURBATION TREATMENT OF DIRECTLY DIPOLE-DIPOLE COUPLED DEGENERATE FREE-ROTOR PRODUCT STATES AT LARGE SEPARATIONS

Here we consider the situation that the strength of the dipole-dipole interaction W_{12}, Eq. (3), between two polar rotors is much smaller than the rotational constant B such that from Eq. (5) we have

$$\widetilde{W}_{12}\sim\Gamma=\frac{\mu^2}{4\pi\epsilon_0R^3B}\ll1 \tag{C1}$$

which occurs when the distance between two rotors R is sufficiently large, i.e. $R\gg1$ nm. It can be shown that the field-free degenerate product states $|m\rangle\otimes|\pm(m+1)\rangle$ and $|m+1\rangle\otimes|\pm m\rangle$, $m=-M,\cdots,-1,0,+1,\cdots,M-1$ (for $M\geq2$), can be grouped into 2-, 2-, and 4-fold irreducible degenerate subspaces (with the degenerate energy equal to $(2m^2+2m+1)B$, see below). These

degenerate energy levels, belonging to 2-, 2-, 4-fold subspaces, respectively, are split (as a result of the perturbation due to the direct dipole-dipole interaction W_{12}) into 2, 2, and 4 sublevels (of energy differences on the order of $\Gamma \sim 1/R^3$, which is much smaller than 1, cf. Eq. (C1)) at large separations. These nearly degenerate sublevels determine the extreme long time field-free recurring patterns of the field-free orientation of the weakly coupled rotors, for example, at $R = 10$ nm and $R = 50$ nm displayed in Fig. 10. All other field-free degenerate product states are not directly coupled by the dipole-dipole interaction $\widetilde{W}_{12}$.

1. The perturbed two-fold degenerate subspaces

$$\mathcal{S}_1^{[2]}(m) \equiv \left\{ |m,(m+1)\rangle\,,\ |(m+1),m\rangle \right\}, \tag{C2}$$

associated with the eigenvalue $\left(2m^2+2m+1\right)B$, where

$$m = -M,\ldots,-2,+1,\cdots,M-1,$$

in turn form a $(2(2M-2))$-dimensional subspace

$$\mathcal{S}_1^{[2(2M-2)]} = \mathcal{S}_1^{[2]}(-M)\oplus\cdots\oplus\mathcal{S}_1^{[2]}(-2)\oplus\mathcal{S}_1^{[2]}(+1)\oplus\cdots\oplus\mathcal{S}_1^{[2]}(+M), \tag{C3}$$

where $'\oplus'$ denotes the direct product of subspaces. The 2×2 dipole-dipole coupling matrix $w_1^{[2]}(m)$ between the two degenerate states of the subspace $\mathcal{S}_1^{[2]}(m)$ can be written as

$$\begin{aligned} w_1^{[2]}(m) &= \begin{pmatrix} \langle m+1,m|\,W_{12}\,|m+1,m\rangle & \langle m+1,m|\,W_{12}\,|m,m+1\rangle \\ \langle m,m+1|\,W_{12}\,|m+1,m\rangle & \langle m,m+1|\,W_{12}\,|m,m+1\rangle \end{pmatrix} \\ &= \frac{1}{4}\Gamma\times\begin{pmatrix} 0 & -1 \\ -1 & 0 \end{pmatrix}. \end{aligned} \tag{C4}$$

It can be shown that by diagonalizing the 2×2 matrix $w_1^{[2]}(m)$, the initially degenerate levels within each subspace $\mathcal{S}_1^{[2]}(m)$ split into two non-degenerate sublevels, respectively, corresponding to energy shifts

$$-\frac{1}{4}\Gamma,\ +\frac{1}{4}\Gamma. \tag{C5}$$

2. The perturbed two-fold degenerate subspaces

$$\mathcal{S}_2^{[2]}(m) \equiv \left\{ |m,-(m+1)\rangle\,,\ |(m+1),-m\rangle \right\}, \tag{C6}$$

associated with the eigenvalue $\left(2m^2+2m+1\right)B$, where

$$m=-M,\ldots,-2,+1,\cdots,M-1.$$

form a $2(2M-2)$-dimensional subspace

$$\mathcal{S}_2^{[2(2M-2)]}=\mathcal{S}_2^{[2]}(-M)\oplus\cdots\oplus\mathcal{S}_2^{[2]}(-2)\oplus\mathcal{S}_2^{[2]}(+1)\oplus\cdots\oplus\mathcal{S}_2^{[2]}(+M). \tag{C7}$$

The 2×2 dipole-dipole coupling matrix $w_2^{[2]}(m)$ between the two degenerate states of the subspace $\mathcal{S}_2^{[2]}(m)$ can be written as

$$\begin{aligned} w_2^{[2]}(m)&=\begin{pmatrix} \langle m,-(m+1)|\,W_{12}\,|m,-(m+1)\rangle & \langle m,-(m+1)|\,W_{12}\,|m+1,-m\rangle \\ \langle m+1,-m|\,W_{12}\,|m,-(m+1)\rangle & \langle m+1,-m|\,W_{12}\,|m+1,-m\rangle \end{pmatrix} \\ &=\frac{1}{4}\Gamma\times\begin{pmatrix} 0 & -3\exp(i2\theta) \\ -3\exp(-i2\theta) & 0 \end{pmatrix}. \end{aligned} \tag{C8}$$

It can shown that by diagonalizing the 2×2 matrix $w_2^{[2]}(m)$, the initially degenerate levels within each subspace $\mathcal{S}_2^{[2]}(m)$ split into a pair of non-degenerate sublevels, respectively, corresponding to energy shifts

$$-\frac{3}{4}\Gamma,\ +\frac{3}{4}\Gamma. \tag{C9}$$

3. The perturbed four-fold degenerate subspace:

$$\mathcal{S}_3^{[4]}\equiv\left\{|-1,0\rangle,\ |0,-1\rangle,\ |0,1\rangle,\ |1,0\rangle\right\}, \tag{C10}$$

associated with the eigenvalue B. The 4×4 dipole-dipole coupling matrix $w_3^{[4]}$ between these four degenerate states can be written as

$$w_3^{[4]}=\frac{1}{4}E_D\times\begin{pmatrix} 0 & -1 & -3\exp(i2\theta) & 0 \\ -1 & 0 & 0 & -3\exp(i2\theta) \\ -3\exp(-i2\theta) & 0 & 0 & -1 \\ 0 & -3\exp(-i2\theta) & -1 & 0 \end{pmatrix} \tag{C11}$$

within the degenerate subspace $\mathcal{S}_3^{[4]}$. It can be shown that the the matrix $w_3^{[4]}$ possesses four distinct eigenvalues $-\Gamma$, $-\frac{1}{2}\Gamma$, $\frac{1}{2}\Gamma$, and Γ, indicating a slight splitting of the initially degenerate levels into four non-degenerate sublevels, respectively.

4. The unperturbed $[(2M+1)^2 - 4(2M-1)]$-dimensional subspace

$$\mathcal{S}_{\emptyset}^{\left[(2M+1)^2-4(2M-1)\right]} \equiv \left\{ |m_1\rangle \otimes |m_2\rangle \notin \mathcal{S}_1^{[4M-4]} \oplus \mathcal{S}_2^{[4M-4]} \oplus \mathcal{S}_3^{[4]} \right\} \tag{C12}$$

is a Hilbert space spanned by all other field-free product states that do not belong to the degenerate subspaces $\mathcal{S}_1^{[2(2M-2)]}$, $\mathcal{S}_2^{[2(2M-2)]}$, and $\mathcal{S}_3^{[4]}$.

APPENDIX D: THE FIELD-FREE OF LONG-TIME REVIVAL PATTERN OF THE ORIENTATION PEAKS

In the absence of the control field and at large separations where

$$\widetilde{W}_{12} \sim \Gamma = \frac{\mu^2}{4\pi\epsilon_0 R^3 B} \ll 1 \tag{D1}$$

it is advantageous to cast the corresponding time-dependent state wave function of the field-free coupled rotors as

$$|\psi^0(\tau)\rangle = \exp\left(-i\left[L_1^2 + L_2^2\right]\tau\right)|\psi_I^0(\tau)\rangle. \tag{D2}$$

Substituting Eq.(D2) in Eq.(8) leads to the governing time-dependent equation

$$i\frac{\partial\left|\psi_I^0(\tau)\right\rangle}{\partial\tau} = W_{12}^I(\tau)\left|\psi_I^0(\tau)\right\rangle, \quad |\psi_I^0(0)\rangle = |\psi(0)\rangle, \tag{D3}$$

in the interaction representation, where

$$W_{12}^I(\tau) = \exp\left(i\left[L_1^2 + L_2^2\right]\tau\right) \times \widetilde{W}_{12} \times \exp\left(-i\left[L_1^2 + L_2^2\right]\tau\right). \tag{D4}$$

It can then be shown that Eq. (D3) may be further approximated as

$$i\frac{\partial}{\partial\tau}\left|\psi_I^0(t)\right\rangle \approx \overline{W}_{12}^I\left|\psi_I^0(\tau)\right\rangle, \tag{D5}$$

analogous to dropping the highly oscillatory terms in the rotating wave approximation [54], where the effective *time-average* dipole-dipole coupling $\overline{W}_{12}^I(\tau)$ is given as

$$\overline{W}_{12}^I \equiv \frac{1}{2\pi}\int_0^{2\pi} W_{12}^I(\tau)d\tau. \tag{D6}$$

The matrix elements of the time-average dipole-dipole interaction $\overline{W}_{12}^I$ can be written as

$$\begin{aligned}&\left\langle m_1 m_2 \left|\overline{W}_{12}^I\right| m_1', m_2'\right\rangle \\ &= \begin{cases} \langle m_1 m_2|\widetilde{W}_{12}|m_1 \pm 1, m_2 \pm 1\rangle & \text{for } m_1' = m_1 \pm 1, m_2' = m_2 \pm 1,, \\ 0 & \text{otherwise,} \end{cases}\end{aligned} \tag{D7}$$

after substituting Eq. (D4) into Eq. (D6). Note that Eq. (D5) has been derived by invoking the integral relation

$$\frac{1}{2\pi}\int_0^{2\pi} \exp\left(-i\left[\left(m_1'^2+m_2'^2\right)-\left(m_1^2+m_2^2\right)\right]\tau\right)d\tau = \begin{cases} 1 & \text{for } \left(m_1'^2+m_2'^2\right)-\left(m_1^2+m_2^2\right)=0 \\ 0 & \text{for } \left(m_1'^2+m_2'^2\right)-\left(m_1^2+m_2^2\right)\neq 0, \end{cases} \tag{D8}$$

for effectively removing highly oscillatory components, relative to the dipole-dipole interaction Γ, of two free rotors. Consequently, we arrive at the approximation for the field-free wave function

$$|\psi^0(\tau)\rangle \approx \exp\left(-i\left[L_1^2+L_2^2\right]\tau\right)\times\exp\left(-i\overline{W}_{12}^I\tau\right)|\psi(0)\rangle, \tag{D9}$$

and find that the evolution of orientation (here for rotor 1) may be *approximated* as

$$\begin{aligned}\langle\cos\varphi_1\rangle(\tau) &\equiv \left\langle\psi^0(\tau)\left|\cos\varphi_1\right|\psi^0(\tau)\right\rangle \\ &= \left\langle\psi_{\rm MOS}\left|\exp\left(+i\overline{W}_{12}^I\tau\right)\times\exp\left(+i\left[L_1^2+L_2^2\right]\tau\right)\cos\varphi_1\right.\right. \\ &\qquad \left.\left.\exp\left(-i\left[L_1^2+L_2^2\right]\tau\right)\times\exp\left(-i\overline{W}_{12}^I\tau\right)\right|\psi_{\rm MOS}\right\rangle. \end{aligned} \tag{D10}$$

with the maximally oriented states $|\psi_{\rm MOS}\rangle$ as the initial state $|\psi(0)\rangle$. From Eq. (D7), and the orthogonal relation $\langle m_i|m_i'\rangle=\delta_{m_i m_i'}$, we can explicitly expand Eq. (D10) as

$$\begin{aligned}\langle\cos\varphi_1\rangle(\tau) = &\sum_{m_1}\sum_{m_2}\sum_{m_1'=m_1\pm1}\sum_{m_1''=m_1\pm1}\sum_{m_2''=m_2\pm1}\sum_{m_1'''=m_1'\pm1}\sum_{m_2'''=m_2\pm1} \\ &\left\langle\psi_{\rm MOS}\left|m_1'',m_2''\right\rangle\times\left\{\left\langle m_1'',m_2''\left|\exp\left(+i\overline{W}_{12}^I\tau\right)\right|m_1,m_2\right\rangle\times\langle m_1|\cos\varphi_1|m_1'\rangle\right.\right. \\ &\times\left.\left\langle m_1',m_2\left|\exp\left(-i\overline{W}_{12}^I\tau\right)\right|m_1''',m_2'''\right\rangle\right\}\times\left\langle m_1''',m_2'''\left|\psi_{\rm MOS}\right\rangle\right. \\ &\times\exp\left(-i\left[m_1'^2-m_1^2\right]\tau\right). \end{aligned} \tag{D11}$$

The field-free orientation dynamics in Eq. (D11) at large separations contain two disparate time scales: (i) short-time fast oscillations, of time scale on the order of the inverse of the rotational constant , and (ii) long time slow modulations, of time scale on the order of the inverse of the dipole-dipole coupling strength $\sim 1/\Gamma \sim R^3$, see Eq. (D7). The long time revival periods in Figs. 10(a) and 10(b) can be understood in terms of the small splittings of the degenerate free-rotor product states due to the very small dipole-dipole coupling $\Gamma \sim 1/R^3$. Specifically, the short-time fast oscillations in Eq. (D11) are due to the exponential term

$$\exp\left(-i[m_1'^2-m_1^2]\tau\right),\ m_1'=m_1\pm1,$$

with $[m_1'^2 - m_1^2] = [(m_1 \pm 1)^2 - m_1^2] \neq 0$, while the long-time slow oscillations are associated with the concatenated products

$$\begin{aligned}
&\left\langle m_1'' m_2'' \left| \left\{ \exp\left(+i\overline{W}_{12}^I \tau\right) \right| m_1, m_2 \right\rangle \times \langle m_1 | \cos\varphi_1 | m_1' \rangle \times \left\langle m_1', m_2 \left| \exp\left(-i\overline{W}_{12}^I \tau\right) \right\} \right| m_1''' m_2''' \right\rangle \\
&= \frac{1}{2} \left\langle m_1'' m_2'' \left| \left\{ \exp\left(+i\overline{W}_{12}^I \tau\right) \right| m_1, m_2 \right\rangle \times \left\langle m_1', m_2 \left| \exp\left(-i\overline{W}_{12}^I \tau\right) \right\} \right| m_1''' m_2''' \right\rangle \\
&\times \left\{ \delta_{m_1, m_1'+1} + \delta_{m_1, m_1'-1} \right\}, \qquad \text{(D12)}
\end{aligned}$$

which indicate only the immediate neighboring free-rotor product states are linked by the joint actions of the dipole-like orientation operator $\cos\varphi_1$ and the time-average dipole-dipole interaction $\overline{W}_{12}^I$. Using the coupling property of the time-average dipole-dipole interaction $\overline{W}_{12}^I$ (as a small perturbation) in Eq. (D7), it was found that the degenerate product states directly coupled by W_{12} can be divided into three distinct subspaces as follows (see Appendix C):

(i) $\mathcal{S}_1^{[2(2M-2)]} \equiv \left\{ \{|m, m+1\rangle,\ |m+1, m\rangle\};\ \ m = -M, \cdots, -2, +1, \cdots, M-1 \right\}$,

(ii) $\mathcal{S}_2^{[2(2M-2)]} \equiv \left\{ \{|m, -m-1\rangle,\ |m+1, -m\rangle\};\ \ m = -M, \cdots, -2, +1, \cdots, M-1 \right\}$,

and

(iii) $\mathcal{S}_3^{[4]} \equiv \left\{ |-1, 0\rangle,\ |0, -1\rangle,\ |0, 1\rangle,\ |1, 0\rangle \right\}$.

Each of two subspaces, $\mathcal{S}_1^{[2(2M-2)]}$ and $\mathcal{S}_2^{[2(2M-2)]}$, is a 2(2M-2)-dimensional one composed of $2M-2$ two-fold degenerate subspaces, while the subspace $\mathcal{S}_3^{[4]}$ is a four-fold degenerate subspace. Thus, the time-average dipole-dipole coupling matrix $\overline{W}_{12}^I$ may be written in a direct-sum (denoted by "$\oplus$") block structure, i.e.,

$$\overline{W}_{12}^I = \widetilde{W}_1^{[2(2M-2)]} \oplus \widetilde{W}_2^{[2(2M-2)]} \oplus \widetilde{W}_3^{[4]} \oplus \widetilde{W}_{\emptyset}^{\left[(2M+1)^2 - 4(2M-1)\right]}, \qquad \text{(D13)}$$

where $\widetilde{W}_1^{[2(2M-2)]}$ and $\widetilde{W}_2^{[2(2M-2)]}$ are direct sums of $2M-2$ sub-blocks of 2×2 *similar* matrices, respectively, Eqs. (C4) and (C8), associated with subspaces $\mathcal{S}_1^{[2(2M-2)]}$ and $\mathcal{S}_2^{[2(2M-2)]}$, $\widetilde{W}_3^{[4]}$ is a 4×4 matrix, Eq. (C11), associated with subspace $\mathcal{S}_3^{[4]}$, while $\widetilde{W}_{\emptyset}^{\left[(2M+1)^2-4(2M-1)\right]}$ is a $[(2M+1)^2 - 4(2M-1)] \times [(2M+1)^2 - 4(2M-1)]$ *zero* matrix defined in the subspace $\mathcal{S}_{\emptyset}^{[(2M+1)^2-4(2M-1)]}$ spanned by all other unperturbed free-rotor product states, including all degenerate ones that are not directly coupled by $\widetilde{W}_{12}$, cf. Eq. (D7). As a result of the small dipole-dipole coupling $\widetilde{W}_{12} \sim \Gamma$, it can be shown that (i) the two-fold degenerate free-rotor product states $|m, m+1\rangle$ and $|m+1, m\rangle$ are split into two sublevels, respectively, corresponding to energy shifts $-\Gamma/4$ and $+\Gamma/4$, (ii) the two-fold degenerate free-rotor product states $|m, -m-1\rangle$ and $|m+1, -m\rangle$ are split into two sublevels, respectively, corresponding to energy shifts $-3\Gamma/4$ and $+3\Gamma/4$, and (iii) the four-fold degenerate free-rotor product states $|-1, 0\rangle$, $|0, -1\rangle$, $|0, 1\rangle$, and $|1, 0\rangle$ are split into four sublevels, respectively,

corresponding to energy shifts, $-\Gamma$,$-\Gamma/2$, $+\Gamma/2$, and $+\Gamma$. A closer examination shows that the quantity

$$|m_1, m_2\rangle\langle m_1| \cos\varphi_1 |m_1'\rangle\langle m_1', m_2|$$

in Eq. (D11) reduces to

$$|m_1, m_2\rangle\langle m_1 \pm 1, m_2|,$$

indicating that the summation over the index m_1' in Eq. (D11) can only assume a value of either m_1+1 or m_1-1; thus, the dipole-like orientation operator $\cos\varphi_1$ only links the perturbed subspaces $\mathcal{S}_1^{[2(2M-2)]}$, $\mathcal{S}_2^{[2(2M-2)]}$, and $\mathcal{S}_3^{[4]}$, individually, to the unperturbed subspace $\mathcal{S}_\emptyset^{[(2M+1)^2-4(2M-1)]}$. Moreover, since the exponential of the zero matrix is an identity matrix, the time-average dipole-dipole evolution operator $\exp\left(-i\overline{W}_{12}^I\tau\right)$ in Eq. (D11) can be written as a direct sum:

$$\begin{aligned}\exp\left(-i\overline{W}_{12}^I\tau\right) &= \exp\left(-i\widetilde{W}_1^{[2(2M-2)]}\tau\right) \oplus \exp\left(-i\widetilde{W}_2^{[2(2M-2)]}\tau\right) \oplus \exp\left(-i\widetilde{W}_3^{[4]}\tau\right) \\ &\quad \oplus \exp\left(-i\widetilde{W}_\emptyset^{[(2M+1)^2-4(2M-1)]}\tau\right) \\ &= \exp\left(-i\widetilde{W}_1^{[2(2M-2)]}\tau\right) \oplus \exp\left(-i\widetilde{W}_2^{[2(2M-2)]}\tau\right) \oplus \exp\left(-i\widetilde{W}_3^{[4]}\tau\right) \\ &\quad \oplus \mathbb{I}_\emptyset^{[(2M+1)^2-4(2M-1)]}, \end{aligned} \tag{D14}$$

where $\mathbb{I}_\emptyset^{[(2M+1)^2-4(2M-1)]}$ is an identity matrix belonging to the subspace $\mathcal{S}_\emptyset^{[(2M+1)^2-4(2M-1)]}$. As a result, there are *four* likely long-time overlapping revival patterns at the asymptotic regime $\Gamma \to 0$, corresponding to the periods

$$T_{\rm L},\ \frac{T_{\rm L}}{2},\ \frac{T_{\rm L}}{3},\ \frac{T_{\rm L}}{4}, \tag{D15}$$

respectively, in the field-free orientation dynamics of the coupled rotors. To this end, we found that (i) sublevels in $\mathcal{S}_1^{[2(2M-2)]}$ are responsible for the longest revival period

$$T_{\rm L} \equiv T_{\rm L}(R) = \frac{4}{\Gamma} \times \tau_{\rm rot} = \frac{8\pi}{\Gamma}, \tag{D16}$$

(ii) sublevels in $\mathcal{S}_2^{[2(2M-2)]}$ contribute to a revival period equal to $T_{\rm L}/3$, while (iii) sublevels in $\mathcal{S}_3^{[4]}$ account for two more revival periods $T_{\rm L}/4$ and $T_{\rm L}/2$. Note that the rotational period for a planar rotor is $\tau_{\rm rot} = 2\pi$ in the dimensionless time.

[1] A. P. Peirce, M. A. Dahleh, and H. Rabitz, Phys. Rev. A **37**, 4950 (1988).

[2] S. Shi, A. Woody, and H. Rabitz, J. Chem. Phys. **88**, 6870 (1988).

[3] R. Kosloff, S. Rice, P. Gaspard, S. Tersigni, and D. Tannor, Chem. Phys. **139**, 201 (1989).

[4] J. Somlói, V. A. Kazakov, and D. J. Tannor, Chem. Phys. **172**, 85 (1993).

[5] W. Zhu and H. Rabitz, J. Chem. Phys. **109**, 385 (1998); W. Zhu, J. Botina, and H. Rabitz, J. Chem. Phys. 108, 1953 (1998).

[6] Y. Maday and G. Turinici, J. Chem. Phys. **118**, 8191 (2003).

[7] Y. Ohtsuki, G. Turinici, and H. Rabitz, J. Chem. Phys. **120**, 5509 (2004).

[8] T.-S. Ho and H. Rabitz, Phys. Rev. E **82**, 026703 (2010); S.-L. Liao, T.-S. Ho, S.-I Chu, and H. Rabitz, Phys. Rev. A 84, 031401(R) (2011).

[9] D. M. Reich, M. Ndong, and C. P. Koch, J. Chem. Phys. **136**, 104103 (2012).

[10] W. Warren, H. Rabitz, and M. Dahleb, Science **259**, 1581 (1993); H. Rabitz, R. de Vivie-Riedle, M. Motzkus, and K. Kompa, Science **288**, 824 (2000).

[11] I. V. Litvinyuk, K. F. Lee, P. W. Dooley, D. M. Rayner, D. M. Villeneuve, and P. B. Corkum, Phys. Rev. Lett. **90**, 233003 (2003); T. Suzuki, S. Minemoto, T. Kanai, and H. Sakai, Phys. Rev. Lett. **92**, 133005 (2004).

[12] H. Stapelfeldt, H. Sakai, E. Constant, P.B. Corkum, Phys. Rev. Lett. **79**, 2787 (1997).

[13] R. Velotta, N. Hay, M. B. Mason, M. Castillejo, and J. P. Marangos, Phys. Rev. Lett. **87**, 183901 (2001); M. Tudorovskaya and M. Lein, Phys. Rev. A **84**, 013430 (2011).

[14] A. M. Childs, E. Farhi, and J. Preskill, Phys. Rev. A **65**, 012322 (2001); E. Farhi *et al*., Science **292**, 472 (2001); D. A. Lidar, A. T. Rezakhani, A. Hamma, J. Math. Phys. **50**, 102106 (2009).

[15] K. Hoki and Y. Fujimura, Chem.Phys. **267**, 187(2001).

[16] J. Salomon, C.M. Dion and G. Turinici, J. Chem. Phys. **123**, 144310 (2005).

[17] S.-H. Liao, T.-S. Ho, H. Rabitz and S.-I Chu, Phys. Rev. A **87**, 013429 (2007).

[18] K. Nakajima, H. Abe and Y. Ohtsuki, J. Phys. Chem. A, **116**, 11219 (2012); M. Yoshida and Y. Ohtsuki, Phys. Rev. A **90**, 013415 (2014); M. Yoshida and Y. Ohtsuki, Chem. Phys. Lett, **633**, 169 (2015).

[19] A. Goban, S. Minemoto, and H. Sakai, Phys. Rev. Lett. **101**, 013001 (2008).

[20] S. Fleischer, Y. Zhou, R. W. Field, and K. A. Nelson, Phys. Rev. Lett. **107**, 163603 (2011).

[21] K. N. Egodapitiya, Sha Li, and R. R. Jones, Phys. Rev. Lett. **112**, 103002 (2014).

[22] J. H. Nielsen, H. Stapelfeldt, J. Küpper, B. Friedrich, J. J. Omiste, and R. González-Férez, Phys. Rev. Lett. **108**, 193001 (2012); S. Trippel, T. Mullins, N. L. M. Müller, J. S. Kienitz, R. González-Férez, and J. Küpper Phys. Rev. Lett. **114**, 103003 (2015).

[23] I. Sh. Averbukh and R. Arvieu, Phys. Rev. Lett. **87**, 163601 (2001); M. Leibscher, I. Sh. Averbukh, and H. Rabitz, Phys. Rev. Lett. **90**, 213001 (2003); W. H. Oskay, D. A. Steck, and M. G. Raizen, Phys. Rev. Lett. **89**, 283001 (2002).

[24] H. Shima and T. Nakayama, Phys. Rev. B **69**, 035202 (2004); H. Shima and T. Nakayama, Phys. Rev. A **70**, 013401 (2004).

[25] M. A. Nielsen, I. Chuang, Quantum Computation and Quantum Information, Cambridge University Press, Cambridge, England, 2000.

[26] C. Hettich, C. Schmitt, J. Zitzmann, S. Kuhn, I. Gerhardt and V. Sandoghdar, Science **398**, 385(2002).

[27] Y. Y. Liao, Y. N. Chen, D. S. Chuu, Chem. Phys. Lett. **398** (2004) 418; Y. Y. Liao, Y. N. Chen, C. M. Li and D. S. Chuu, J. Phys. B: At. Mol. Opt. Phys. **39**, 421 (2006).

[28] E. Charron, P. Milman, A. Keller, and O. Atabek,Phys. Rev. A **75**, 033414(2007).

[29] K. Mishima and K. Yamashita, Inter. J. Quan. Chem. **108**, 1352(2008); K. Mishima and K. Yamashita, J. Chem. Phys. **130**, 034108 (2009); K. Mishima and K. Yamashita, Chem. Phys. **361**, 106 (2009); K. Mishima and K. Yamashita, Chem. Phys. **379**, 13 (2011).

[30] J. Zhu, S. Kais, Q. Wei, D. Herschbach and B. Friedrich, J. Chem. Phys. **138**, 024104 (2013); M. Karra, K. Sharma, B. Friedrich, S. Kais and D. Herschbach, J. Chem. Phys. **144**, 094301 (2016).

[31] R. T. Kidd, D. Lennon, and S. R. Meech, J. Chem. Phys. 113, 8276 (2000); T. Vondrak, D. J. Burke, and S. R. Meech, Chem. Phys. Letts. **347**, 1 (2001).

[32] D. Demille, Phys. Rev. Lett. **88**, 067901(2002).

[33] S. Kotochigova and E. Tiesinga, Phys. Rev. A **73**, 041405(R) (2006).

[34] N. Bouloufa, O. Dulieu, H. Ritsch, and H.-C. Nägerl, Science **321**, 1026 (2008).

[35] K.-K. Ni, S. Ospelkaus, M. H. G. de Miranda, A. Pe'er,1 B. Neyenhuis, J. J. Zirbel, S. Kotochigova, P. S. Julienne, D. S. Jin, and J. Ye, Science **322**, 231 (2008).

[36] A. Rothman, T.-S. Ho and H. Rabitz, J. Chem. Phys. **123**, 134104 (2005); A. Rothman, T.-S. Ho and H. Rabitz, Phys. Rev. A **72**, 023416 (2005); A. Rothman, T.-S. Ho, and H. Rabitz, Phys. Rev. A **73**, 053401 (2006).

[37] F. Yang, S. Cong, R. Long, T.-S. Ho, R. Wu and H. Rabitz, Phys. Rev. A **88**, 033420(2013).

[38] J. Yan, D. Hocker, R. Long, T.-S. Ho, and H. Rabitz, Phys. Rev. A **89**, 063408 (2014).

[39] C. Joe-Wong, T.-S. Ho, H. Rabitz, J. Chem. Phys. **142**, 154115 (2015).

[40] C.-C. Shu, T.-S. Ho, X. Xi, H. Rabitz, Phys. Rev. A **93**, 033417 (2016); C.-C. Shu, T.-S. Ho, H. Rabitz, Phys. Rev. A **93**, 053418 (2016).

[41] M. B. Plenio and S. Virmani, Quantum Inf. Comput. **7**, 1 (2007); L. Amico, R. Fazio, A. Osterloh, and V. Vedral, Rev. Mod. Phys. **80**, 517 (2008); R. Horodecki, P. Horodecki, M. Horodecki, and K. Horodecki, Rev. Mod. Phys. **81**, 865 (2009); M. C. Tichy, F. Mintert, and A. Buchleitner, J. Phys. B: At. Mol. Opt. Phys. **44**, 192001 (2011).

[42] W. H. Press, S. A. Teukolsky, W. T. Vetterling, B. P. Flannery, *Numerical Recipes*, 3rd ed. (Cambridge University Press, 2007), Chapter 17.

[43] I. S. Lin, J. D.Mckinney, A. M. Weiner, IEEE Microwave and Wireless Components Lett **15**, 226 (2005); J. Yao, Optics Commu. **284**, 3723 (2011)

[44] H. Rabitz, M. Hsieh, and C. Rosenthal, Science **303**, 1998 (2004); H. Rabitz, T.-S. Ho, M. Hsien, R. Kosut, and M. Demiralp, Phys. Rev. A **74**, 012721 (2006); T.-S. Ho and H. Rabitz, J. Photochem. Photobiol. A: Chem. **180**, 226 (2006).

[45] B. Russell, H. Rabitz, and R. Wu, J. Phys. A: Math. Theor. **50**, 205302 (2017).

[46] A. G. Maki, J. Phys. Chem. Ref. Data **3**, 221 (1974).

[47] R. G. Shulman and C. H. Townes, Phys. Rev. **77**, 500 (1950).

[48] S. H. Gold and G. S. Nusinovich, Rev. Sci. Instrum. **68**, 3945 (1997); J. H. Booske, Phys. Plasmas **15**, 055502 (2008); F. Hamamah, W. F. H. Wan Ahmad, C. Gomes, M. Mohd Isa, and M. J. Homam, Proceeding of 2017 Asia Pacific Microwave Conference, page 825.

[49] M. Machholm and N. E. Henriksen, Phys. Rev. Lett. **87**, 193001 (2001).

[50] M. Lapert and D. Sugny, Phys. Rev. A **85**, 063418 (2012).

[51] J. Werschnik and E. K. U. Gross, J. Opt. B **7**, S300 (2005); Y. Kurosaki, M. Artamonov, T.-S. Ho, and H. Rabitz, J. Chem. Phys. **131**, 044306 (2009); T. Blasi, M. F. Borunda, E. Räsänen, and E. J. Heller, Phys. Rev. B **87**, 241303(R) (2013); N. I. Shvetsov-Shilovski, L. B. Madsen, and E. Räsänen, Phys. Rev. A **91**, 023425 (2015); D. S. A. Coden, R. H. Romero, A. Ferrôn, and S. S. Gomez, Phys. E **86**, 36 (2017).

[52] J. Federici and L. Moller, J. Appl. Phys. **107**, 143-171 (2011); J. Capmany and D. Novak, Nature Photo., **1**, 319-330 (2007).

[53] S. Noschese, L. Pasquini, and L. Reichel, Numer. Linear Algebra Appl. **20**, 302 (2013).

[54] K. Kormann, S. Holmgren, and H. O. Karlsson, J. Chem. Phys. **128**, 184101 (2008).

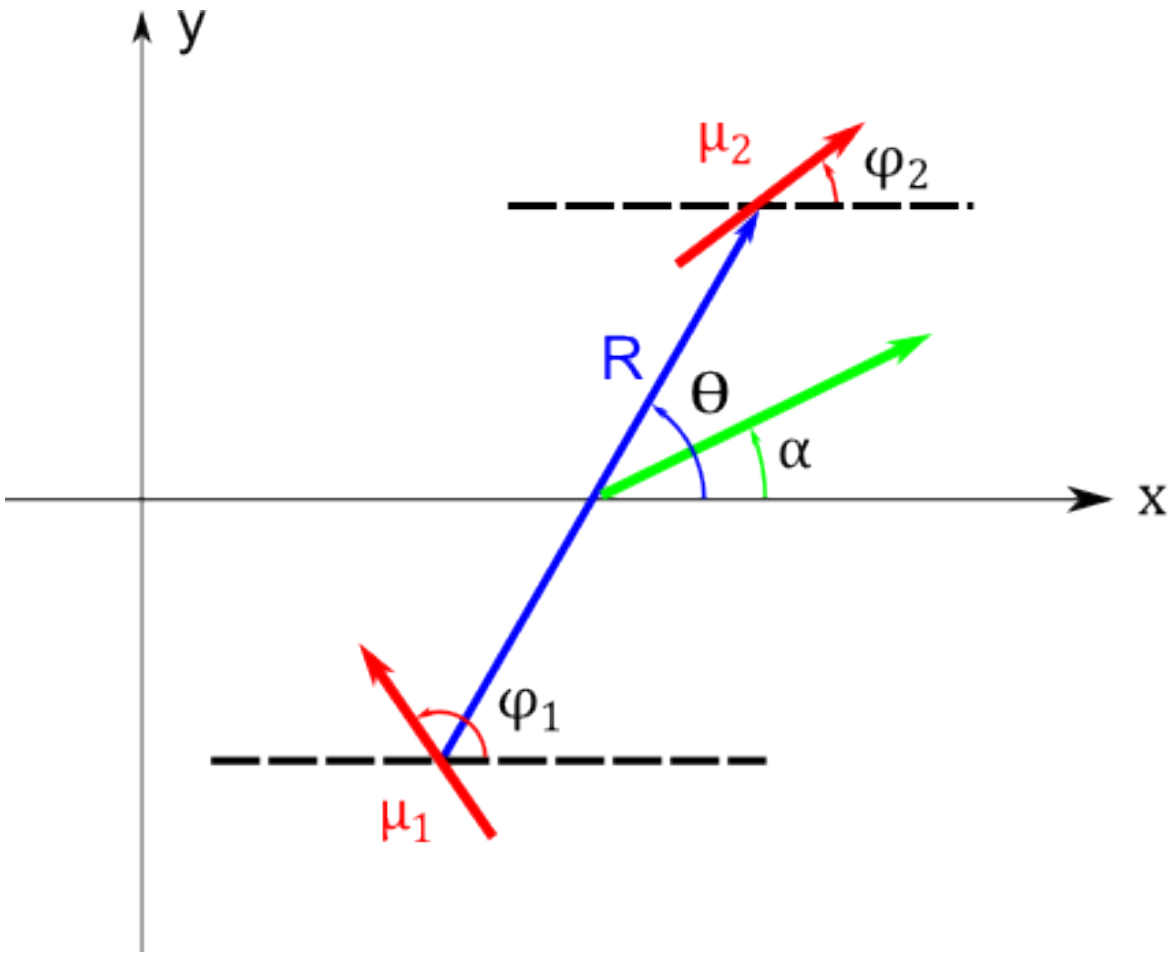

FIG. 1. The sketch shows the configuration of two planar rotors,with dipole moments $\boldsymbol{\mu}_1$ and $\boldsymbol{\mu}_2$ pointing in the directions denoted by the rotor angles $\varphi_1 \in [-\pi, \pi]$ and $\varphi_2 \in [-\pi, \pi]$, respectively, from the $\hat{\mathbf{x}}$-axis. The two rotors are separated by R, the linearly polarized electric field $\varepsilon(t)$ is along the $\hat{\mathbf{x}}$-axis, and the configuration angle between inter-rotor vector $\mathbf{R}$ and the electric field $\varepsilon(t)$ is denoted by $\theta \in [0, \pi/2]$. When orientation is the control goal, the target angle is denoted by $\alpha \in [-\pi/2, \pi/2]$ from the $\hat{\mathbf{x}}$-axis.

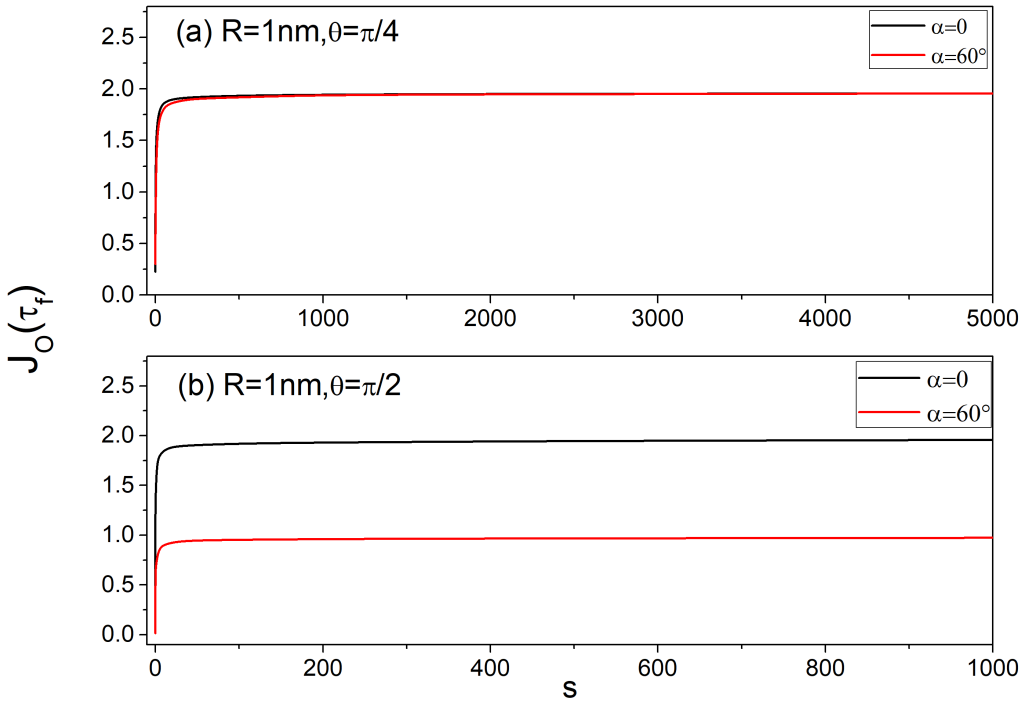

FIG. 2. Plots of the orientation objective functional $J_O(\tau_f)$ vs the optimization parameter s based on the use of D-MORPH for different θ and α at the separation $R = 1$ nm corresponding to strong dipole-dipole coupling and starting with the same initial control field. The initial state $|\psi(0)\rangle$ is the ground state $|E_1\rangle$ of the coupled rotors. The initial control field, Eq. (37), is composed of three frequencies: $\omega_1 = 8.1248$, $\omega_2 = 7.5543$, and $\omega_3 = 6.8751$. It takes about five times the number of optimization steps to reach the maximum expectation value ~ 1.97 of the orientation for (a) the oblique configuration angle $\theta = \pi/4$ than it does for (b) the perpendicular configuration angle $\theta = \pi/2$.

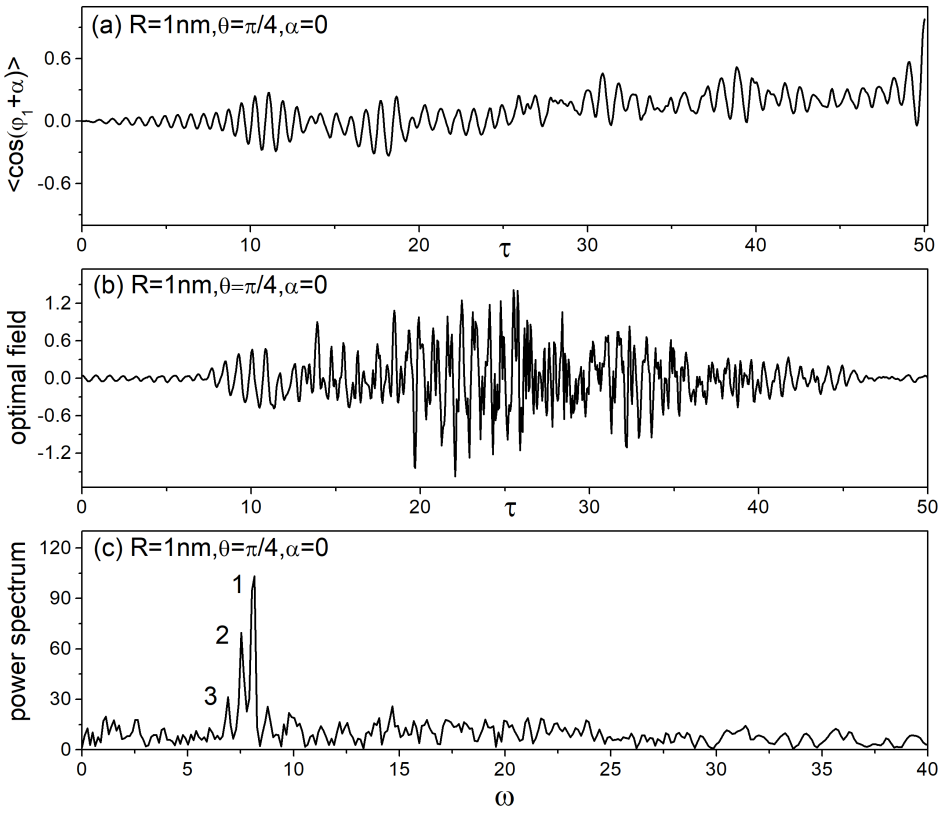

FIG. 3. Orientation control for $\theta = \pi/4$, $\alpha = 0$, and strong dipole-dipole coupling with $R = 1$ nm. (a) The temporal evolution of orientation of rotor 1 (the same for rotor 2) in the presence of optimal control field. (b) The optimal control field, $\varepsilon(\tau)$ (in units of $a_0 = 0.85625\times10^5$ V/cm) as a function of time τ. (c) The power spectrum of the optimal field. The initial state is the ground state $|E_1\rangle$ of the coupled rotors. Three dominant peaks, labeled as $1, 2, 3$ in (c), respectively, corresponding to the frequencies $\omega_1 = 8.1248$, $\omega_2 = 7.5543$, and $\omega_3 = 6.8751$, which coincide with the sequential transitions: $|E_1\rangle \rightarrow |E_7\rangle \rightarrow |E_{14}\rangle \rightarrow |E_{27}\rangle$, used to construct the initial field. The pulse length of the control fields is $\tau_f = 50$.

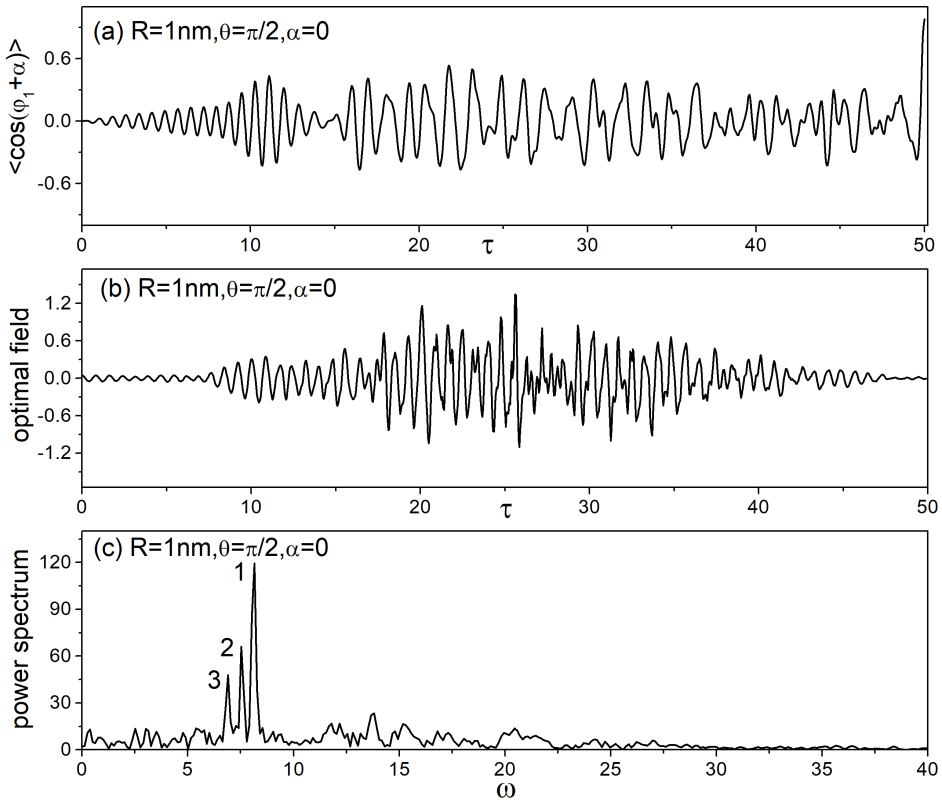

FIG. 4. Orientation control for $\theta = \pi/2$, $\alpha = 0$, and strong dipole-dipole coupling with $R = 1$ nm. (a) The temporal evolution of orientation of rotor 1 (the same for rotor 2) in the presence of optimal control field. (b) The optimal control field, $\varepsilon(\tau)$ (in units of $a_0 = 0.85625\times10^5$ V/cm) as a function of time τ. (c) The power spectrum of the optimal field. The initial state is the ground state $|E_1\rangle$ of coupled rotors. Three dominant peaks, labeled as $1, 2, 3$ in (c), respectively, corresponding to the frequencies $\omega_1 = 8.1248$, $\omega_2 = 7.5543$, and $\omega_3 = 6.8751$, which coincide with the sequential transitions: $|E_1\rangle \rightarrow |E_7\rangle \rightarrow |E_{14}\rangle \rightarrow |E_{27}\rangle$, used to construct the initial field. The pulse length of the control fields is $\tau_f = 50$.

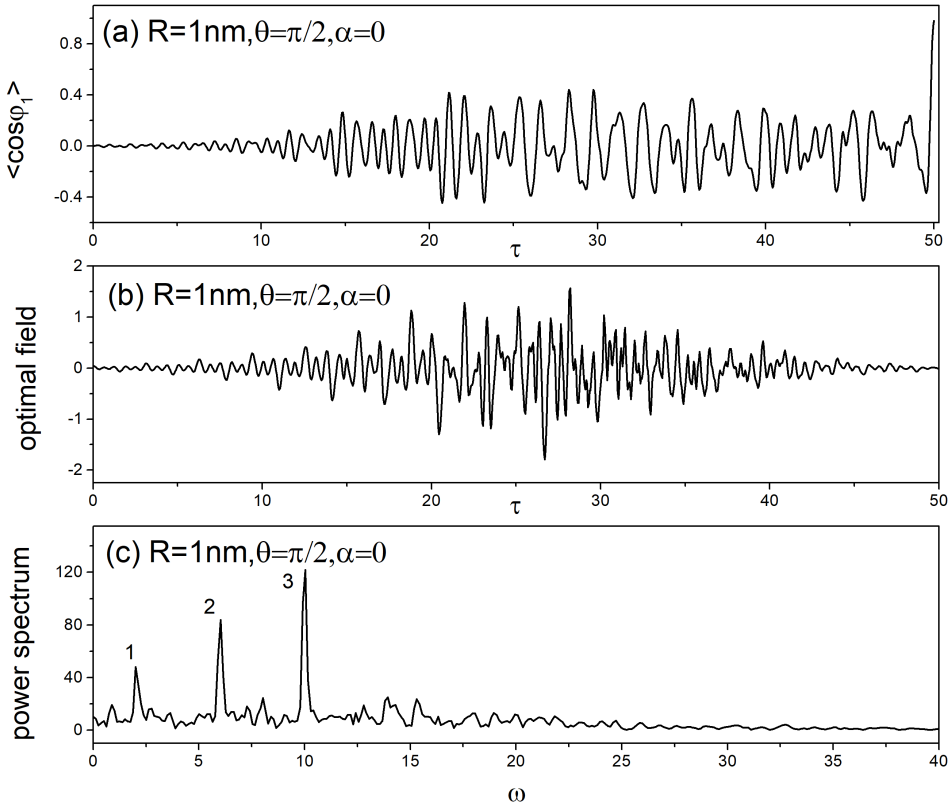

FIG. 5. Orientation control for the case (A2) in the text for $\theta = \pi/2$, $\alpha = 0$, and strong dipole-dipole coupling with $R = 1$ nm. (a) The temporal evolution of orientation of rotor 1 (the same for rotor 2) in the presence of optimal control field. (b) The optimal control field, $\varepsilon(\tau)$ (in units of $a_0 = 0.85625\times10^5$ V/cm) as a function of time τ. (c) The power spectrum of the optimal field.The initial state is the ground state $|E_1\rangle$ of the coupled rotors. Three dominant peaks, labeled as 1, 2, 3 in (c), respectively, corresponding to the frequencies $\omega_1 = 2$, $\omega_2 = 6$, and $\omega_3 = 10$, which coincide with the sequential transitions: $|00\rangle \rightarrow |11\rangle \rightarrow |22\rangle \rightarrow |33\rangle$, used to construct the initial field. The pulse length of the control fields is $\tau_f = 50$.

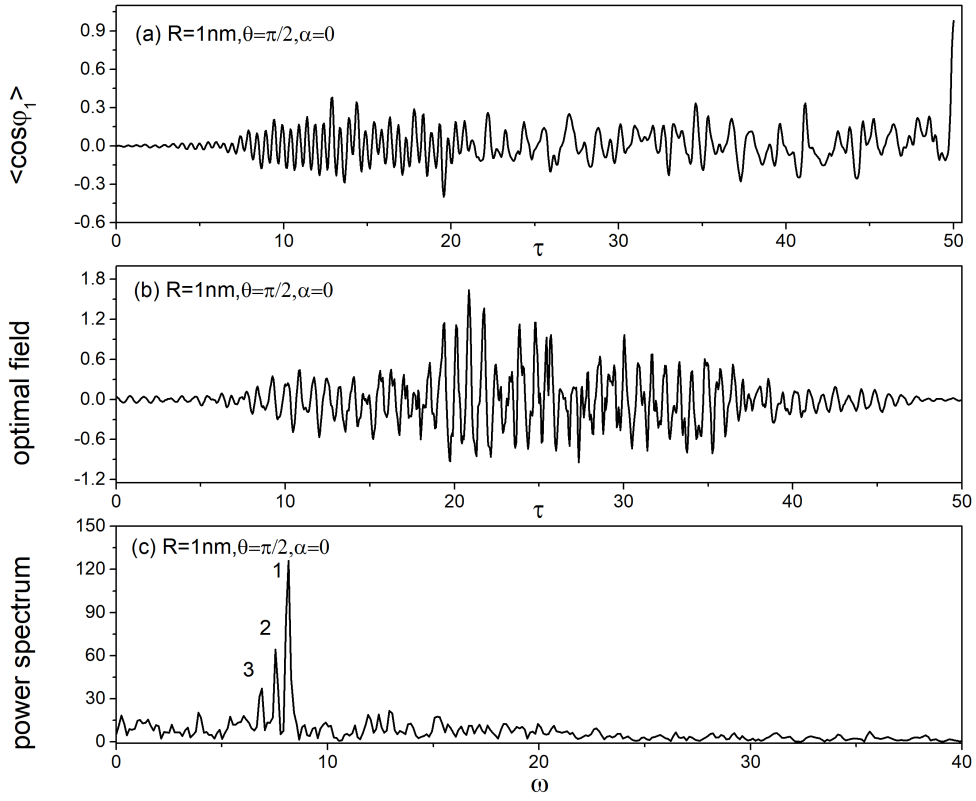

FIG. 6. Orientation control for the case (A3) in the text for $\theta = \pi/2$, $\alpha = 0$, and strong dipole-dipole coupling with $R = 1$ nm. (a) The temporal evolution of orientation of rotor 1 (the same for rotor 2) in the presence of optimal control field. (b) The optimal control field, $\varepsilon(\tau)$ (in units of $a_0 = 0.85625 \times 10^5$ V/cm) as a function of time τ. (c) The power spectrum of the optimal field. The initial state is the ground product state $|0\rangle \otimes |0\rangle$ of the uncoupled rotors. Three dominant peaks, labeled as $1, 2, 3$ in red color in (c), respectively, corresponding to the frequencies $\omega_1 = 8.1248$, $\omega_2 = 7.5543$, and $\omega_3 = 6.8751$, which coincide with the sequential transitions: $|E_1\rangle \rightarrow |E_7\rangle \rightarrow |E_{14}\rangle \rightarrow |E_{27}\rangle$. The pulse length of the control fields is $\tau_f = 50$.

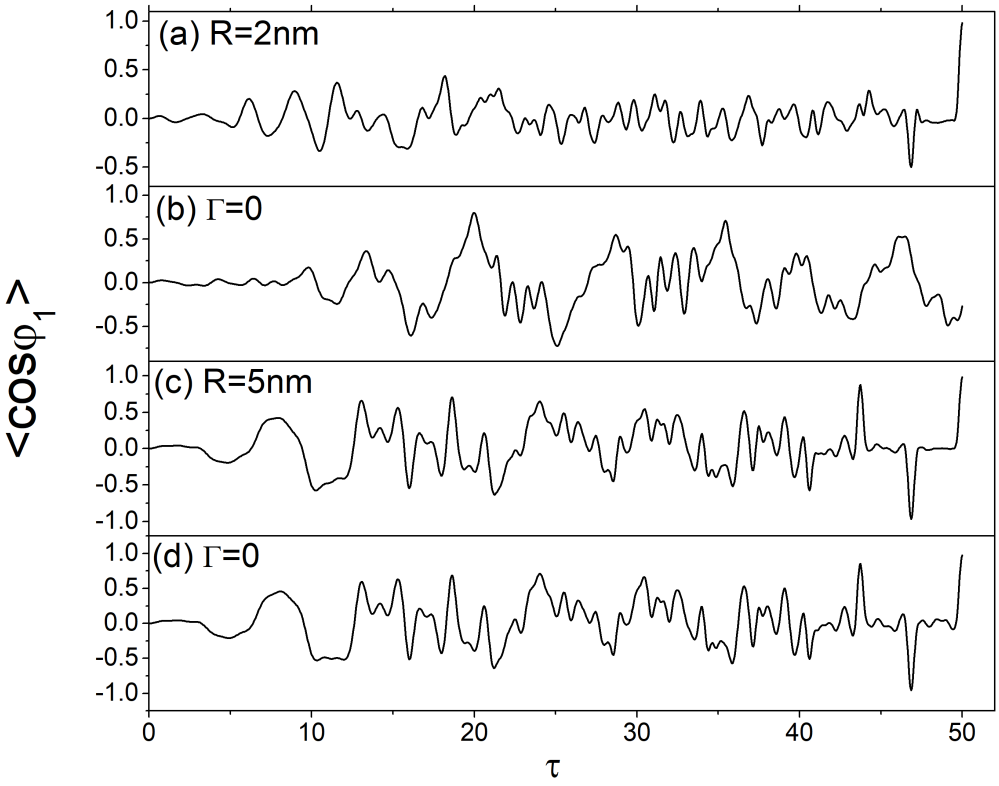

FIG. 7. Time evolution of orientation of the coupled rotors in the presence of their respective optimal fields (not shown), for the perpendicular configuration angle $\theta = \pi/2$, at the target angle $\alpha = 0$ and two separations. Case (a) is at $R = 2$ nm with the intermediate dipole-dipole coupling $\Gamma = 1.55$, and (b) is a free rotor ($\Gamma = 0$) driven by the same optimal control field as in panel (a). Case (c) is $R = 5$ nm at weak dipole-dipole coupling $\Gamma = 0.1$, and (d) shows a free rotor ($\Gamma = 0$) driven by the same optimal control field as in panel (c). The initial state is the ground state $|E_1\rangle$ of the coupled rotors at the respective separations. The initial field $\varepsilon(0, \tau)$ is composed of three frequencies: at $R = 2$ nm, $\omega_1 = 2.2475$, $\omega_2 = 3.5415$, and $\omega_3 = 4.6245$, corresponding to the sequential transitions $|E_1\rangle \rightarrow |E_6\rangle \rightarrow E_{17}\rangle \rightarrow |E_{28}\rangle$ of the coupled rotors, and at $R = 5$ nm, $\omega_1 = 1$, $\omega_2 = 3$, and $\omega_3 = 5$, corresponding to the sequential transitions $|0\rangle \rightarrow |1\rangle \rightarrow 2\rangle \rightarrow |3\rangle$ of a single rotor.

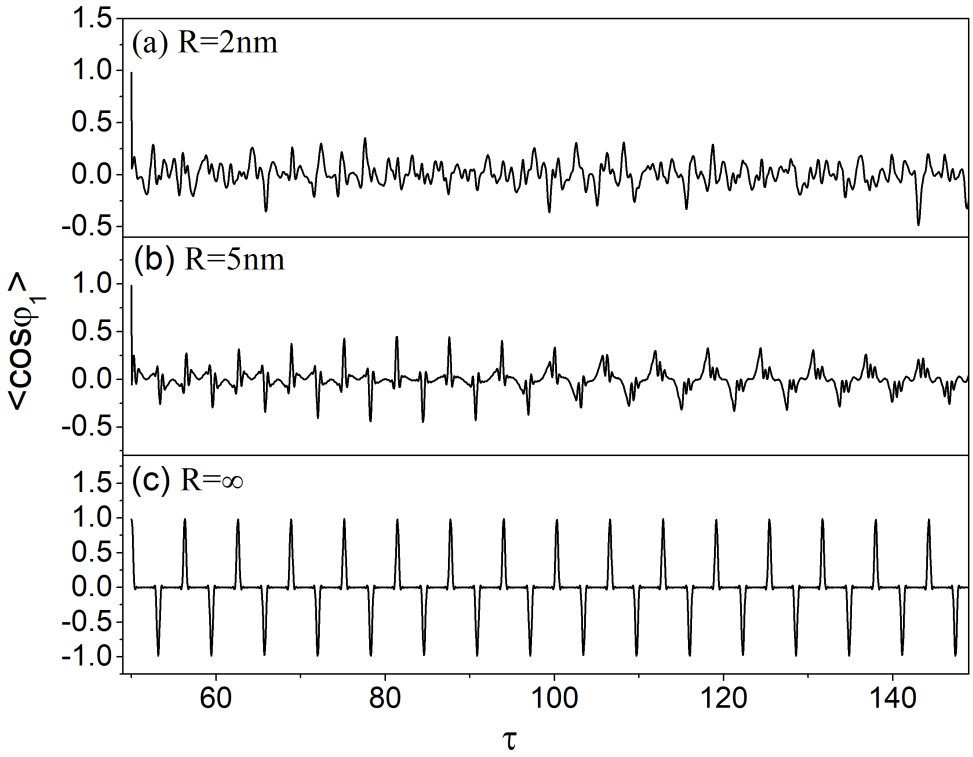

FIG. 8. Time evolution of the field-free orientation of the coupled rotors (starting from the maximally oriented states) at the separations (a) $R = 2$ nm, (b) $R = 5$ nm, and (c) $R = \infty$ (free rotors) for the perpendicular configuration angle $\theta = \pi/2$ and the target angle $\alpha = 0$. Clear revival behavior is evident at weak dipole-dipole coupling (b) and with no coupling (c).

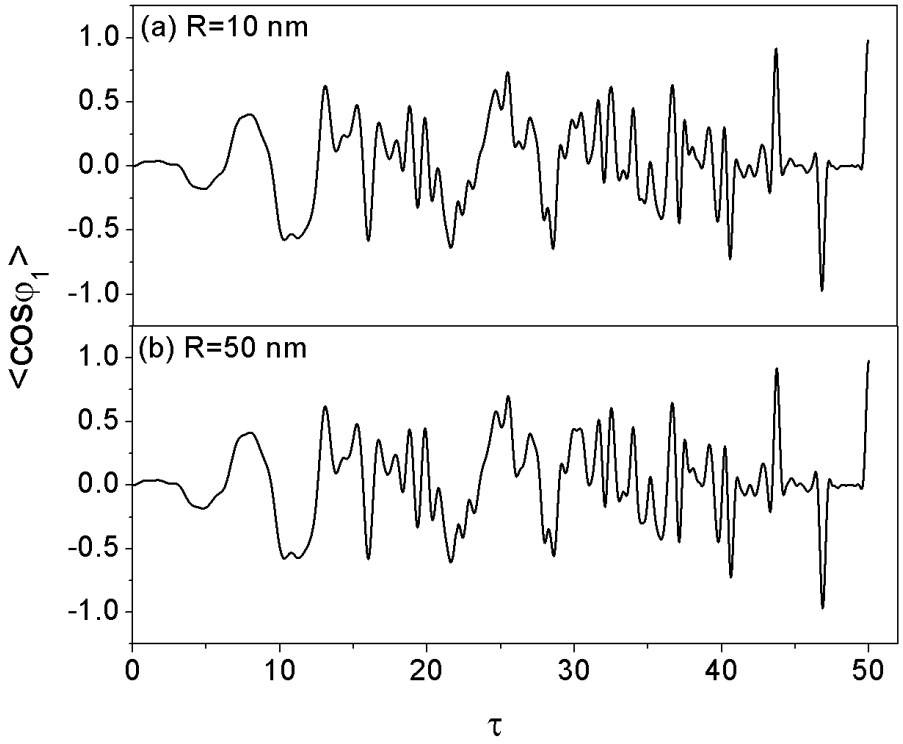

FIG. 9. Time evolution of orientation of the couple rotors in the presence of their respective optimal fields (not shown) at the separations (a) $R = 10$ nm (very weak dipole-dipole coupling) and (b) $R = 50$ nm (extremely weak coupling) for the configuration angle $\theta = \pi/2$ and the target angle $\alpha = 0$. The initial state is the ground state $|E_1\rangle$ of the coupled rotors at the respective separations. The initial field $\varepsilon(0, \tau)$ is composed of three frequencies: $\omega_1 = 1$, $\omega_2 = 3$, and $\omega_3 = 5$, corresponding to the sequential transitions $|0\rangle \rightarrow |1\rangle \rightarrow 2\rangle \rightarrow |3\rangle$ of a single rotor.

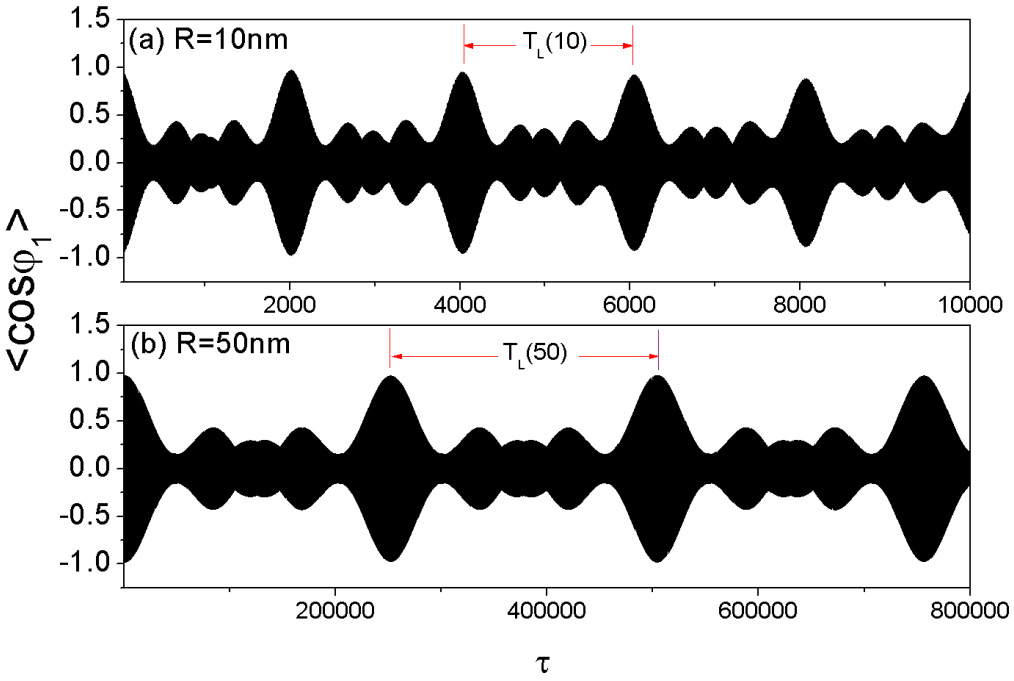

FIG. 10. Long time evolution of the field-free orientation of the coupled rotors (starting from the maximally oriented states) at the separations (a) $R = 10$ nm and (b) $R = 50$ nm for the perpendicular configuration angle $\theta = \pi/2$ and the target angle $\alpha = 0$. The black regions hide the rapid short-period nearly free rotation of the rotors, while the long-time scale beating envelopes arise from the weak perturbation due to the dipole-dipole coupling. The labeled periods $T_L(R)$, $R = 10, 50$, correspond to the primary recurrence features. See the text for details.

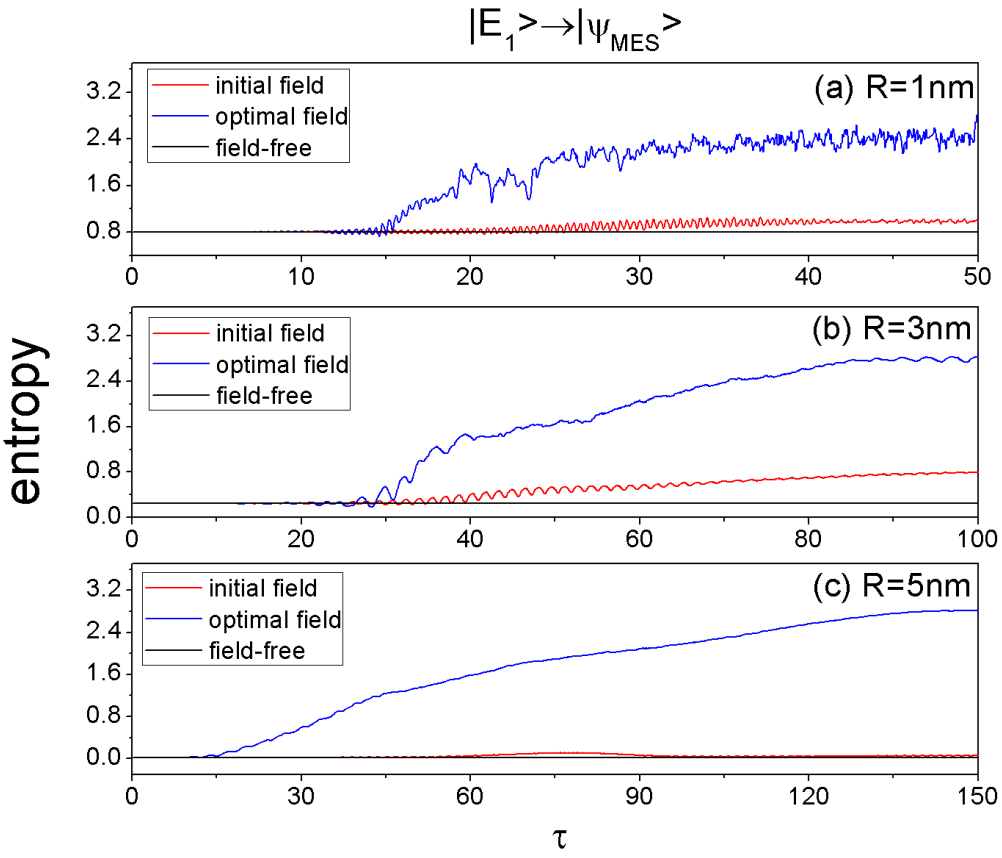

FIG. 11. Time evolution of entanglement entropy, Eq. (23), of the coupled rotors, for the perpendicular configuration $\theta = \pi/2$, in the presence of control fields at different separations and pulse lengths: (a) $R = 1$ nm, $\tau_f = 50$, (b) $R = 3$ nm, $\tau_f = 100$ and (c) $R = 5$ nm, $\tau_f = 150$, after applying three different fields: (1) the initial field(red line) (2) the optimal field(blue line) and (3) in the absence of field(black line), for the transition from state $|E_1\rangle$ to $|\psi_{MES}\rangle$. The initial state is the ground state $|E_1\rangle$ of the coupled rotors at the respective separations.

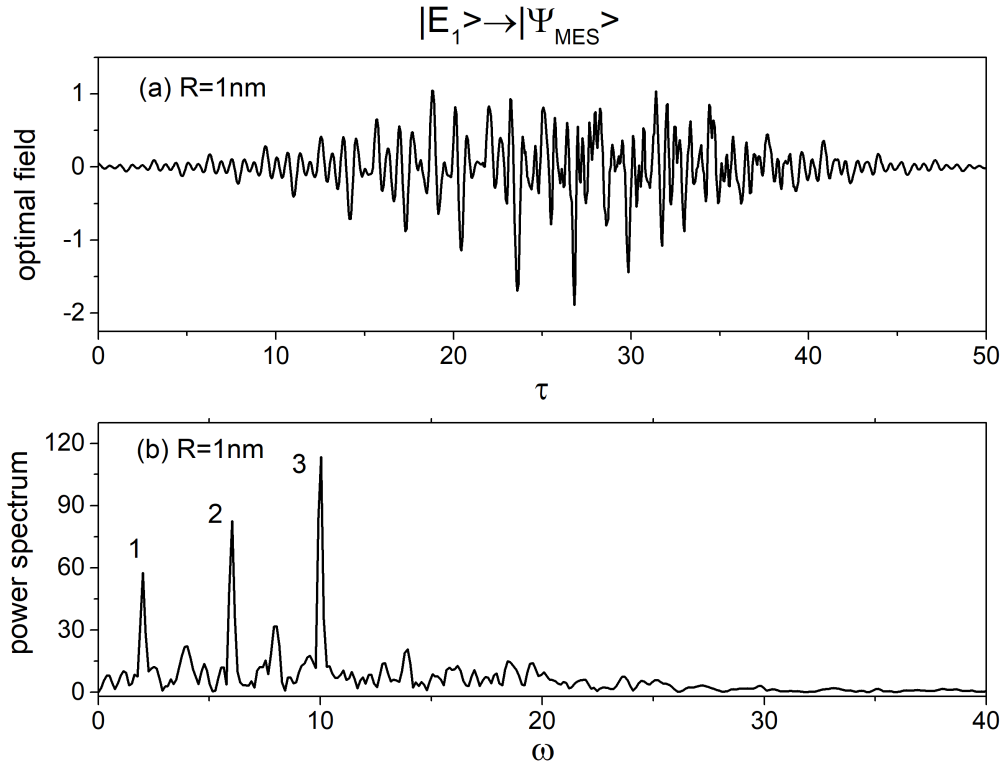

FIG. 12. (a) The optimal field (in units of $a_0 = 0.85625 \times 10^5$ V/cm) and (b) its power spectrum, corresponding to Fig. 11(a), for the perpendicular configuration angle $\theta = \pi/2$ at the separation $R = 1$ nm for the transition from the state $|E_1\rangle$ to the state $|\psi_{\rm MES}\rangle$. Three dominant peaks, labeled as $1, 2, 3$ in (b), respectively, corresponding to the frequencies $\omega_1 = 2$, $\omega_2 = 6$, and $\omega_3 = 10$, which coincide with the sequential transitions between three lowest product states of the two free rotors: $|0\rangle \otimes |0\rangle \rightarrow |1\rangle \otimes |1\rangle \rightarrow |2\rangle \otimes |2\rangle \rightarrow |3\rangle \otimes |3\rangle$.

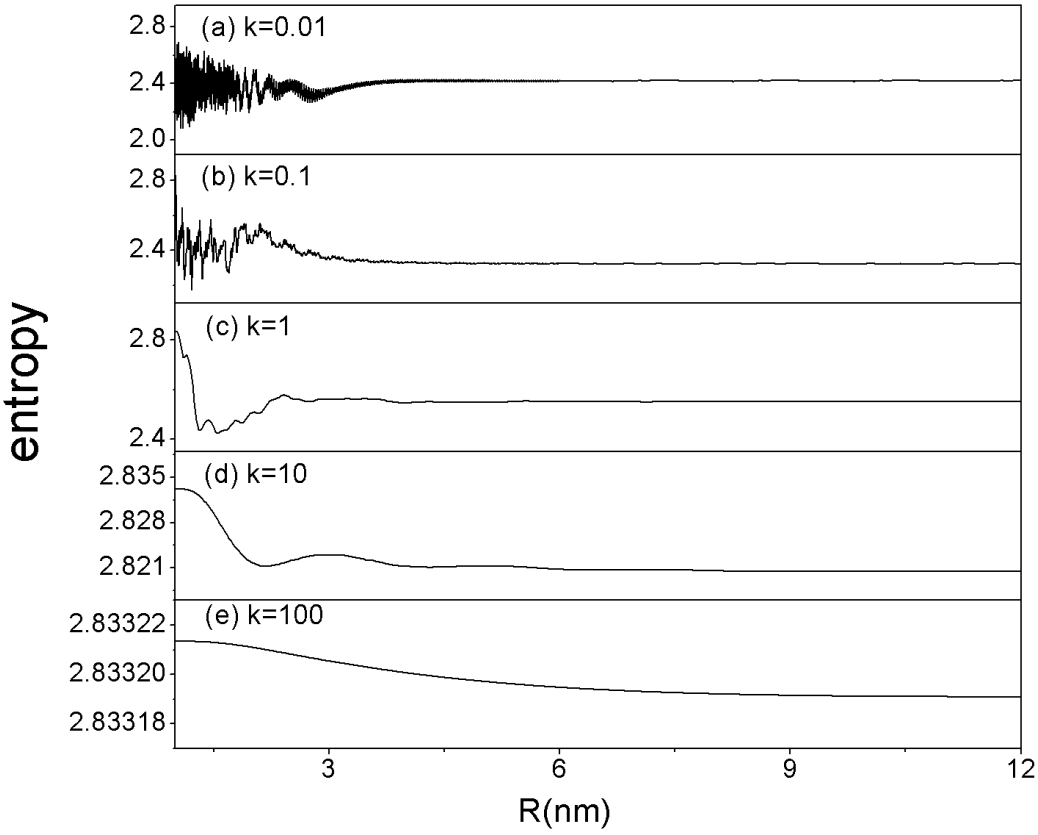

FIG. 13. The field-free entanglement entropy, Eq. (23), of the coupled rotors, for the perpendicular configuration $\theta = \pi/2$ and starting from $|\psi_{\rm MES}\rangle$ at $R = 1$ nm, as a function of R for different separation rates (a) $k = 0.01$ (b) $k = 0.1$ (c) $k = 1$ (d) $k = 10$ and (e) $k = 100$ in Eq. (46). Despite the obvious differences due to the distinct rates of rotor separation, the key observation is that entanglement changes modestly, at most, as the rotors are separated.

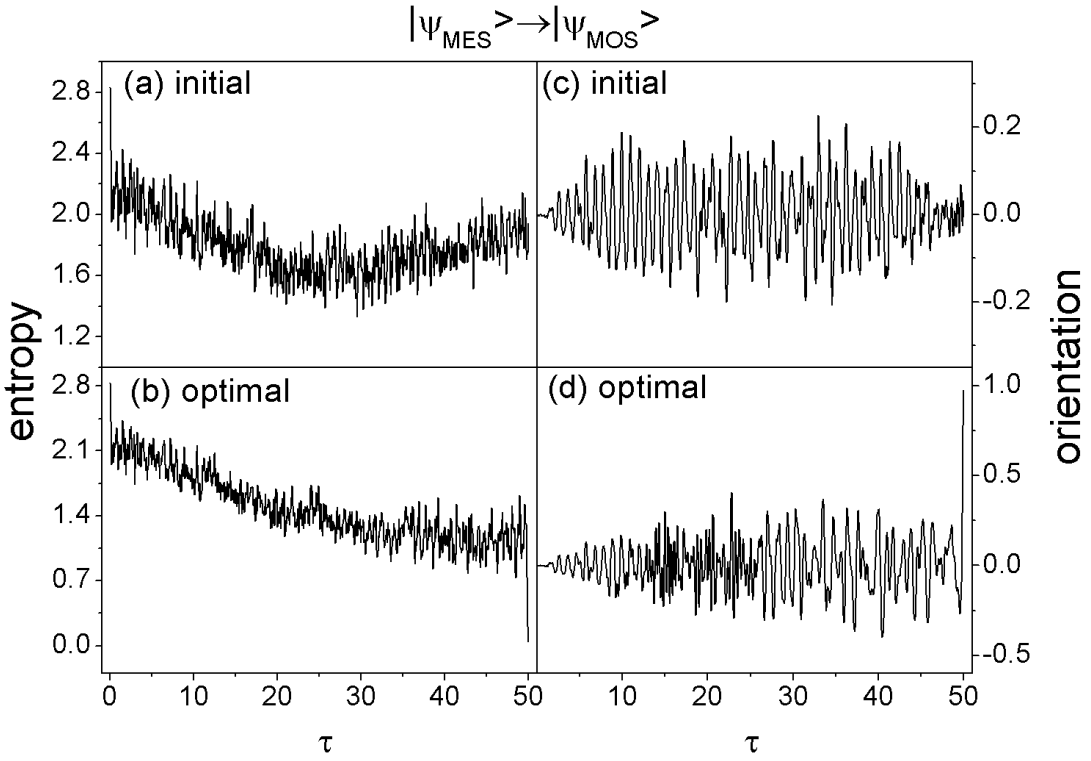

FIG. 14. Time evolution of entanglement entropy (left panels) and orientation (right panels) of the coupled rotors; note the corresponding labeling of the ordinates. The configuration is perpendicular $\theta = \pi/2$, in the presence of the initial field, (a) and (c), and the optimal field, (b) and (d), for the transition $|\psi_{\rm MES}\rangle \rightarrow |\psi_{\rm MOS}\rangle$ at the strong dipole-dipole coupling separation $R = 1$ nm.

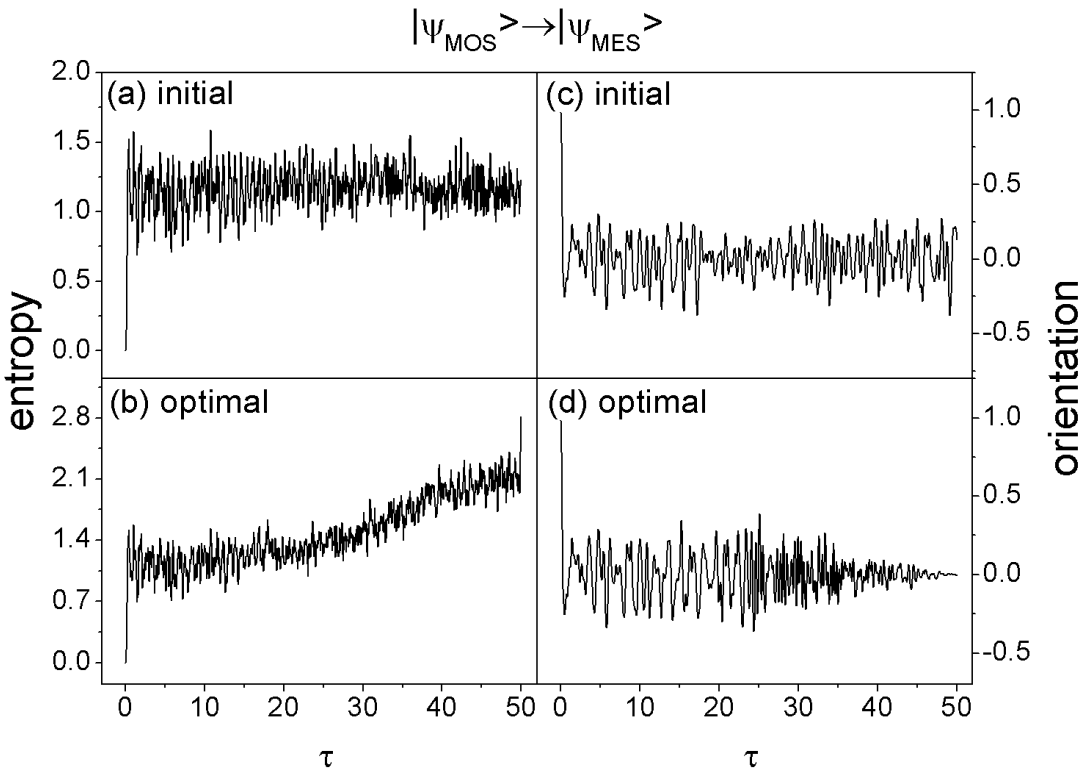

FIG. 15. Time evolution of entanglement entropy (left panels) and orientation (right panels) of the coupled rotors; note the corresponding labeling of the ordinates. The configuration is perpendicular $\theta = \pi/2$, in the presence of the initial field, (a) and (c), and the optimal field, (b) and (d), for the transition from $|\psi_{\rm MOS}\rangle$ to $|\psi_{\rm MES}\rangle$ at the separation $R = 1$ nm.